Resource

Immunity

Primary nasal influenza infection rewires tissue-scale memory response dynamics

Graphical abstract

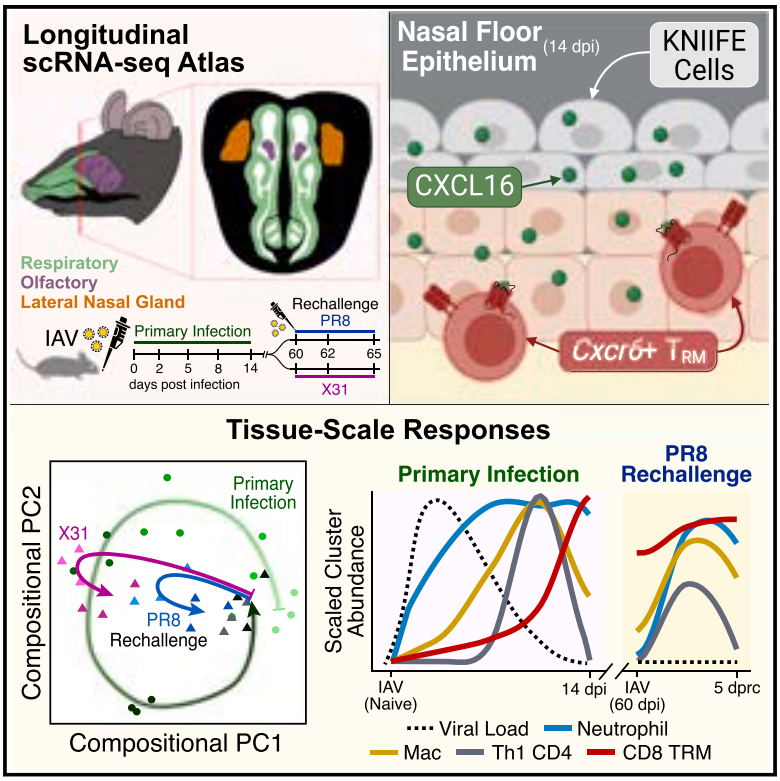

Highlights

- Influenza infection induces stepwise changes in nasal epithelial and immune subsets
- Single-cell compositional analyses reveal coordinated changes in time and space
- *Cxcl16*+ epithelial KNIIFE cells line the nasal floor near *Cxcr6*$^{+}$ T_{RM} cells
- Nasal viral rechallenge induces rapid and concerted myeloid and T cell responses

Authors

Samuel W. Kazer, Colette Matysiak Match, Erica M. Langan, ..., Katherine Naughton, Ulrich H. von Andrian, Jose Ordovas-Montanes

Correspondence

jose.ordovas-montanes@childrens.harvard.edu

In brief

The nasal mucosa is a key barrier for respiratory infections, but the cellular responses therein are poorly understood. Kazer et al. generate a longitudinal tissue-scale single-cell nasal atlas during IAV infection and rechallenge, identifying unique epithelial subsets responding to infection and revealing highly coordinated myeloid and T cell responses during rechallenge.

Kazer et al., 2024, Immunity *57*, 1–20
August 13, 2024
https://doi.org/10.1016/j.immuni.2024.06.005

CellPress

Immunity

CellPress

Resource

Primary nasal influenza infection rewires tissue-scale memory response dynamics

Samuel W. Kazer,[1,2,3,4,10] Colette Matysiak Match,[3,4,10] Erica M. Langan,[1,2] Marie-Angèle Messou,[3,4] Thomas J. LaSalle,[2,5] Elise O'Leary,[3] Jessica Marbourg,[6] Katherine Naughton,[7] Ulrich H. von Andrian,[3,4,11] and Jose Ordovas-Montanes[1,2,4,8,9,11,12,*]

[1]Division of Gastroenterology, Hepatology, and Nutrition, Boston Children's Hospital, Boston, MA, USA
[2]Broad Institute of MIT and Harvard, Cambridge, MA, USA
[3]Department of Immunology, Harvard Medical School, Boston, MA, USA
[4]Ragon Institute of MGH, MIT and Harvard, Cambridge, MA, USA
[5]Program in Health Sciences and Technology, Harvard Medical School and Massachusetts Institute of Technology, Boston, MA, USA
[6]AbbVie Cambridge Research Center, Cambridge, MA, USA
[7]AbbVie Genomics Research Center, North Chicago, IL, USA
[8]Program in Immunology, Harvard Medical School, Boston, MA 02115, USA
[9]Harvard Stem Cell Institute, Harvard University, Cambridge, MA, USA
[10]These authors contributed equally
[11]Senior author
[12]Lead contact
*Correspondence: jose.ordovas-montanes@childrens.harvard.edu
https://doi.org/10.1016/j.immuni.2024.06.005

SUMMARY

The nasal mucosa is often the initial site of respiratory viral infection, replication, and transmission. Understanding how infection shapes tissue-scale primary and memory responses is critical for designing mucosal therapeutics and vaccines. We generated a single-cell RNA-sequencing atlas of the murine nasal mucosa, sampling three regions during primary influenza infection and rechallenge. Compositional analysis revealed restricted infection to the respiratory mucosa with stepwise changes in immune and epithelial cell subsets and states. We identified and characterized a rare subset of Krt13+ nasal immune-interacting floor epithelial (KNIIFE) cells, which concurrently increased with tissue-resident memory T (T_{RM})-like cells. Proportionality analysis, cell-cell communication inference, and microscopy underscored the CXCL16-CXCR6 axis between KNIIFE and T_{RM} cells. Secondary influenza challenge induced accelerated and coordinated myeloid and lymphoid responses without epithelial proliferation. Together, this atlas serves as a reference for viral infection in the upper respiratory tract and highlights the efficacy of local coordinated memory responses.

INTRODUCTION

As the primary passage to the lower airway, the nasal mucosa balances the complex roles of olfaction, filtration, and conditioning of air with host defense. To accomplish these functions, the nose contains distinct anatomical structures with diverse cell subsets that secrete specialized proteins.[1] In the face of pathogens, the nasal mucosa mounts various incompletely understood defense mechanisms to protect against infection and limit spread to the lower respiratory tract.[2] Nevertheless, many respiratory pathogens circumvent the nose and disseminate into the lungs, causing severe disease, hospitalization, and fatal outcomes.[3–5]

The inflammatory state of nasal tissue affects the viral infection trajectory. The COVID-19 pandemic has emphasized the roles of interferons (IFNs) in nasal protection and disease severity, highlighting the importance of timing, location, viral burden, and strain.[6–9] Single-cell analysis of the human nasopharynx during severe acute respiratory syndrome coronavirus 2 (SARS-CoV-2) infection suggests muted IFN responses in epithelial cells from severe disease relative to mild cases.[10] More generally, evidence of a recent prior infection in children receiving a live-attenuated influenza vaccine is associated with enhanced interferon stimulated gene (ISG) signaling and lower viral shedding.[11] Collectively, this suggests that the cumulative exposure history informs the present nasal state and composition and may drive disease outcomes.[12–17]

Following viral infection or intranasal (i.n.) vaccination, immune memory in the nasal mucosa can provide long-term protection both systemically and at the mucosal barrier, reducing pathology and infection burden in the lower airways and elsewhere.[18–20] Local protection is afforded by both cellular and humoral immune mechanisms. For example, $CD8^+$ tissue-resident memory (T_{RM}) cells that form following upper respiratory tract influenza A virus (IAV) infection correlate with enhanced protection against heterologous IAV strain rechallenge.[21] Protective mucosal

Please cite this article in press as: Kazer et al., Primary nasal influenza infection rewires tissue-scale memory response dynamics, Immunity (2024), https://doi.org/10.1016/j.immuni.2024.06.005

immunoglobulin A (IgA)-producing plasma cells and neutralizing antibodies can be generated in the nasal mucosa following IAV, vesicular stomatitis virus, respiratory syncytial virus (RSV), and SARS-CoV-2 infections.[18,22–25]

To develop protective, durable, and efficacious vaccines for respiratory viruses, we must better understand the establishment, timing, and cooperation of tissue-scale memory following natural infection.[26–28] Immune responses to pathogens often occur in stepwise fashion: recognition of pathogen-associated molecular patterns by immune and/or epithelial cells leads to cytokine production that broadly activates myeloid cells that, in turn, recruit pathogen-specific effector lymphocytes, some of which will develop into circulating and T_{RM} cells.[29] Following prior infection or vaccination, these local circuits can be re-ordered and even inverted in the barrier tissues that re-encounter infection.[14,30–33] During viral rechallenge, T_{RM} cells exhibit antiviral effector functions and can act as sentinels that send antigen-specific inflammatory "alarms" to activate multicellular responses at the site of infection.[33–36] In mucosal vaccination, IFNγ produced by antigen-specific T cells will induce increased inflammatory cytokine production by both distal[37,38] and local[39] antigen-presenting cells, suggesting that recruited and/or tissue-resident cells can contribute to rapid memory responses. Similarly, antibodies can directly neutralize virus and orchestrate various antiviral effector functions through antibody Fc-receptor-mediated binding by natural killer (NK) cells, macrophages, and neutrophils.[40] However, most studies to date have focused on individual roles of cell types or limited interactions during a memory response.

Here, we present a tissue-scale single-cell RNA sequencing (scRNA-seq) atlas of the murine nasal mucosa before and during primary IAV infection and secondary rechallenge. By sampling multiple regions, time points, and cell lineages, we develop a compositional landscape of the tissue and reveal how the diversity of cell subsets and states dynamically changes in response to infection and during a memory response. Primary IAV infection induced stepwise shifts in cell composition, starting with increased IFN-responsive neutrophil subsets followed by broader antiviral/IFN-stimulated responses in epithelial, myeloid, and lymphoid immune cells. Next, monocyte-derived macrophages (MDMs) accumulated along with effector $CD8^+$ and $CD4^+$ T cells. Following viral resolution, early T_{RM} cells and plasmablasts were established alongside increased frequencies of rare Krt13+ nasal immune-interacting floor epithelial (KNIIFE) cells expressing an assortment of genes with immunomodulatory potential. Upon rechallenge, the nasal memory response to IAV is accelerated and coordinated, compared with primary infection, to different degrees based on viral homology. Collectively, our spatial and temporal datasets enumerate and characterize the diversity of cell types, states, and subsets in the murine nasal mucosa and highlight recruited and local cell subsets that exhibit memory and respond to viral infection.

RESULTS

Single-cell spatiotemporal atlas of primary influenza infection in the nasal mucosa

We administered IAV H1N1 PR8 i.n. to awake, naive mice, to restrict infection to the upper respiratory tract,[21,41] and processed nasal mucosa tissue ($n = 3$ biological samples/time point) by scRNA-seq at 0, 2, 5, 8, and 14 days post infection (dpi; primary) (Figure 1A). Anatomically, the murine nasal mucosa can be divided into tissue regions by morphology and function.[1] We mapped the cellular and structural diversity in the naive nasal mucosa by immunofluorescence, observing broad heterogeneity in epithelial, immune, and neural distribution throughout the tissue (Figure 1B). To capture region-specific changes in cell composition and response during IAV infection, we separated the tissue into three regions: (1) respiratory mucosa (RM), inclusive of the nasal and maxillary turbinates, septum, and vomeronasal organ; (2) olfactory mucosa (OM), inclusive of the ethmoid turbinates; and (3) the lateral nasal gland (LNG), which sits in the maxillary sinus.

Across all primary infection time points (0–14 dpi, $n = 45$), we collected 156,572 single-cell transcriptomes. Top-level clustering captured 42 clusters belonging to neural, epithelial, immune, and stromal (endothelial, fibroblast, and others) cell lineages, demarcated by known lineage-restricted genes (Figures 1C and S1A). Neurons and epithelial cells comprised over half of the dataset (Figure S1B). Major cell types were distributed unevenly across regions, with enrichment of neurons, granulocytes, B cells, and hematopoietic stem cells (HSCs) in the OM and more epithelial cells, fibroblasts, myeloid cells, and T and NK cells in the RM (Figures 1D and S1C). As highly structured nasal tissues, the turbinates, and especially the ethmoid turbinate (OM), contain substantial amounts of bone and bone marrow. Thus, the relative enrichment of specific immune cell types, including HSCs and other immune progenitors in the OM, likely reside in this bone marrow and may directly enter the mucosa and engage in pathogen defense[42] (Figure 1B). Sample replicates did not exhibit strong batch effects (Figure S1D). Although clustering was performed on all singlets, only hash-annotated cells were utilized for downstream compositional analyses (Figure S1E).

To delineate the diversity of cell subsets and states in the nasal mucosa, we split the dataset by cell type and conducted new clustering analyses, yielding a total of 127 clusters (Figure S1F; Table S1). By counting the cells assigned to each cluster in each sample replicate and scaling across samples by cell capture, we calculated cell cluster abundances to interrogate the relationship between samples in cell compositional space (STAR Methods; Table S2). Performing principal-component analysis (PCA) on samples over center log-ratio (clr) transformed cell cluster abundances, we saw strong regional separation (Figure 1E). Examination of the PCA loadings revealed that LNG has higher abundances of odorant-binding protein (OBP)-expressing cells, serous cells, and capillary endothelial cells (Figure S1G). OM has relatively more Schwann cells, HSCs, and glandular cells, while RM is enriched for vomeronasal sensory neurons, chondrocytes, and infection-responsive epithelial cells. Collectively, this atlas represents a high-resolution view of the mouse nasal mucosa, enabling characterization of cellular composition dynamics during infection.

Influenza infection is largely restricted to the RM, with reproducible changes in cellular composition

Although viral, immune cell, and epithelial cell dynamics following IAV infection of the lung are partially mapped,[43–47]

Please cite this article in press as: Kazer et al., Primary nasal influenza infection rewires tissue-scale memory response dynamics, Immunity (2024), https://doi.org/10.1016/j.immuni.2024.06.005

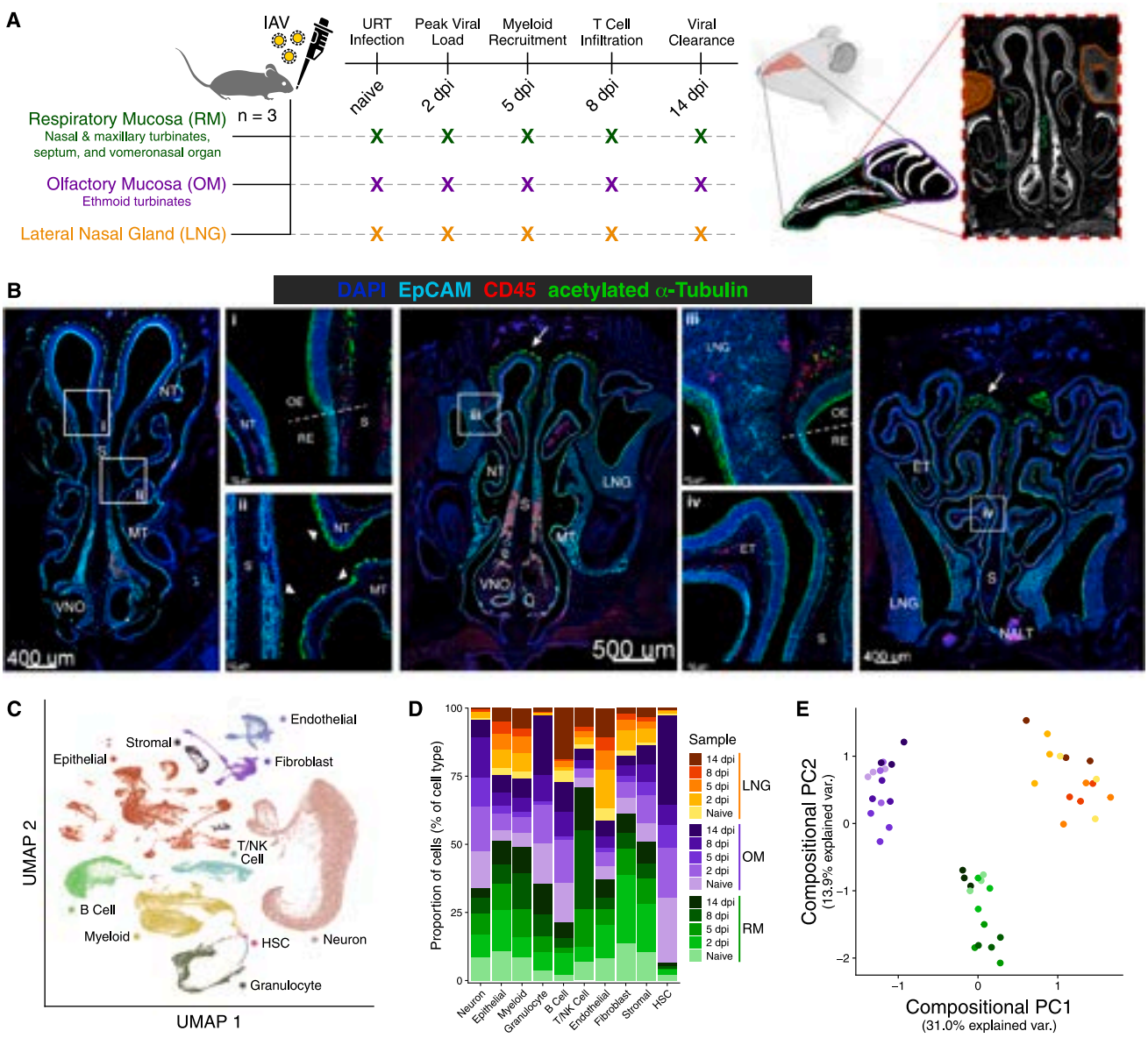

Figure 1. Single-cell atlas of the nasal mucosa during primary IAV infection

(A) Experimental design. Influenza A virus (IAV) was restricted to the nasal mucosa. Dpi, days post infection; RM, respiratory mucosa; OM, olfactory mucosa; LNG, lateral nasal gland.

(B) Representative immunofluorescence images of coronal slices of the nasal mucosa from a naive mouse moving from anterior (left) to dorsal (right) staining for epithelial cells (EpCAM, teal), immune cells (CD45, red), and ciliated cells/neurons (α-acetylated tubulin, green). White arrows point to olfactory sensory nerve bundles; white arrowheads point to cilia. The olfactory epithelium (OE) and respiratory epithelium (RE) both reside within the collected RM tissue and are differentiated by morphology and the presence of olfactory sensory neurons. NT, nasoturbinate; S, septum; MT, maxillary turbinate; VNO, vomeronasal organ; LNG, lateral nasal gland; ET, ethmoid turbinate; and NALT, nasal-associated lymphoid tissue.

(C) Uniform manifold approximation and projection (UMAP) embedding of 156,572 nasal cells across three tissue regions and five time points ($n = 3$ per region/time point) colored by cell type. HSC, hematopoietic stem cell.

(D) Stacked bar chart depicting the relative proportions of cells annotated for each cell type by region and time point.

(E) Compositional principal-component analysis (PCA) of all acute infection sample replicates. Each point represents a sample replicate and distance reflects variation in cell cluster abundance (scaled cell counts). Dots are colored by region and time point as in (B).

the nasal mucosa is less studied. Total nasal mucosa viral titers showed robust infection 2 dpi that waned through 8 dpi and was cleared by 14 dpi (Figure 2A). Lung titers showed sporadic viral spread between 5 and 8 dpi (Figure S2A). Aligning to a joint IAV and mouse genome, we captured viral transcripts by scRNA-seq and identified cells containing viral reads. Individual genes like nucleoprotein (NP) and hemagglutinin (HA) were detected in epithelial and myeloid cells (Figure S2B). We calculated a summative IAV unique molecular identifier (UMI) count for every cell to assess IAV "positivity" (Figure 2B). Across time

Please cite this article in press as: Kazer et al., Primary nasal influenza infection rewires tissue-scale memory response dynamics, Immunity (2024), https://doi.org/10.1016/j.immuni.2024.06.005

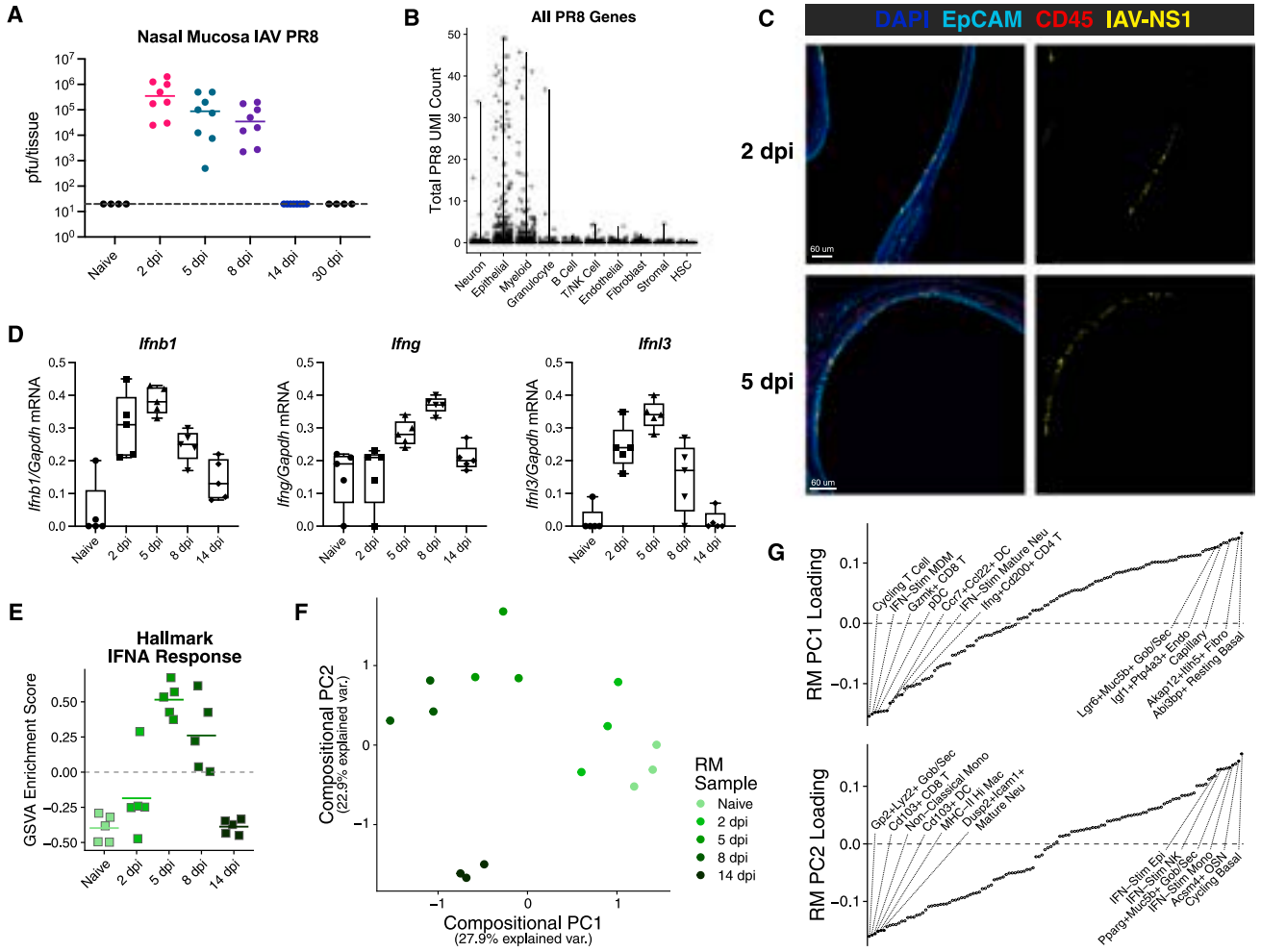

Figure 2. IAV infection induces stepwise changes in RM cellular composition

(A) Infectious IAV PR8 quantification in plaque-forming units (pfu) of the entire nasal mucosa.

(B) Summative scTransform-corrected UMI counts per cell across all IAV PR8 genes.

(C) Representative images of IAV infection in RM taken from mice 2 dpi (top) and 5 dpi (bottom). Staining for EpCAM (teal), CD45 (red), and IAV-NS1 (yellow). Images on the right depict only the signal in the IAV-NS1 channel.

(D) qPCR of *Ifnb1* (left), *Ifng* (center), and *Ifnl3* from RNA extracted from RM tissue. C_q ratios are normalized by *Gapdh* C_q. n = 5/time point.

(E) Gene set variation analysis (GSVA) enrichment score for Hallmark response to IFNα on total RM tissue lysate bulk RNA-seq data (n = 5/time point).

(F) Compositional PCA of all cell clusters from only RM samples.

(G) Cell cluster abundance loadings for PC1 and PC2 from (F). Cell cluster names for several of the most negative and most positive weights for each PC are depicted.

points and regions, we captured low, but reproducible, numbers of IAV+ cells 2–8 dpi in the RM aligning with positive plaque assays (Figures S2C and S2D). Bulk RNA-seq of whole RM tissue lysate better matched the plaque-forming assay results, with higher IAV read counts than single-cell sequencing, suggesting non-cellular viral RNA and/or potential loss of IAV+ cells during scRNA-seq processing (Figure S2E).

Staining for IAV NS1 at 2 and 5 dpi confirmed that infection was largely restricted to epithelial cells in the RM (Figures 2C, S2F, and S2G), consistent with expression of binding receptors marked by α2,3-linked sialic acid in mucus-producing cells.[48] We performed qPCR of total RM to validate an early response to infection and found robust induction of type I and III IFNs 2 dpi, with higher expression 5 dpi despite lower viral titers (Figure 2D). *Ifng* expression exhibited delayed kinetics, peaking at 8 dpi. To understand the global IFN-induced response dynamics during infection, we calculated response enrichment scores to IFNα and IFNγ from bulk RNA-seq data (Figures 2E and S2H). Despite elevated levels of *Ifnb1* at 2 dpi, IFN-response signaling was not enriched until 5 dpi; however, we cannot exclude that IFN responses occur between 2 and 5 dpi, given sampling limitations.

To understand how infection remodels each nasal region, we applied PCA to the sample replicates within each region. In OM, 5- and 14-dpi samples separated from each other and the other time points (Figure S2I). In LNG, only 14-dpi samples separated from the rest (Figure S2J). Comparatively, the RM PCA showed clear separation between all time points in chronological

Please cite this article in press as: Kazer et al., Primary nasal influenza infection rewires tissue-scale memory response dynamics, Immunity (2024), https://doi.org/10.1016/j.immune.2024.06.005

CellPress

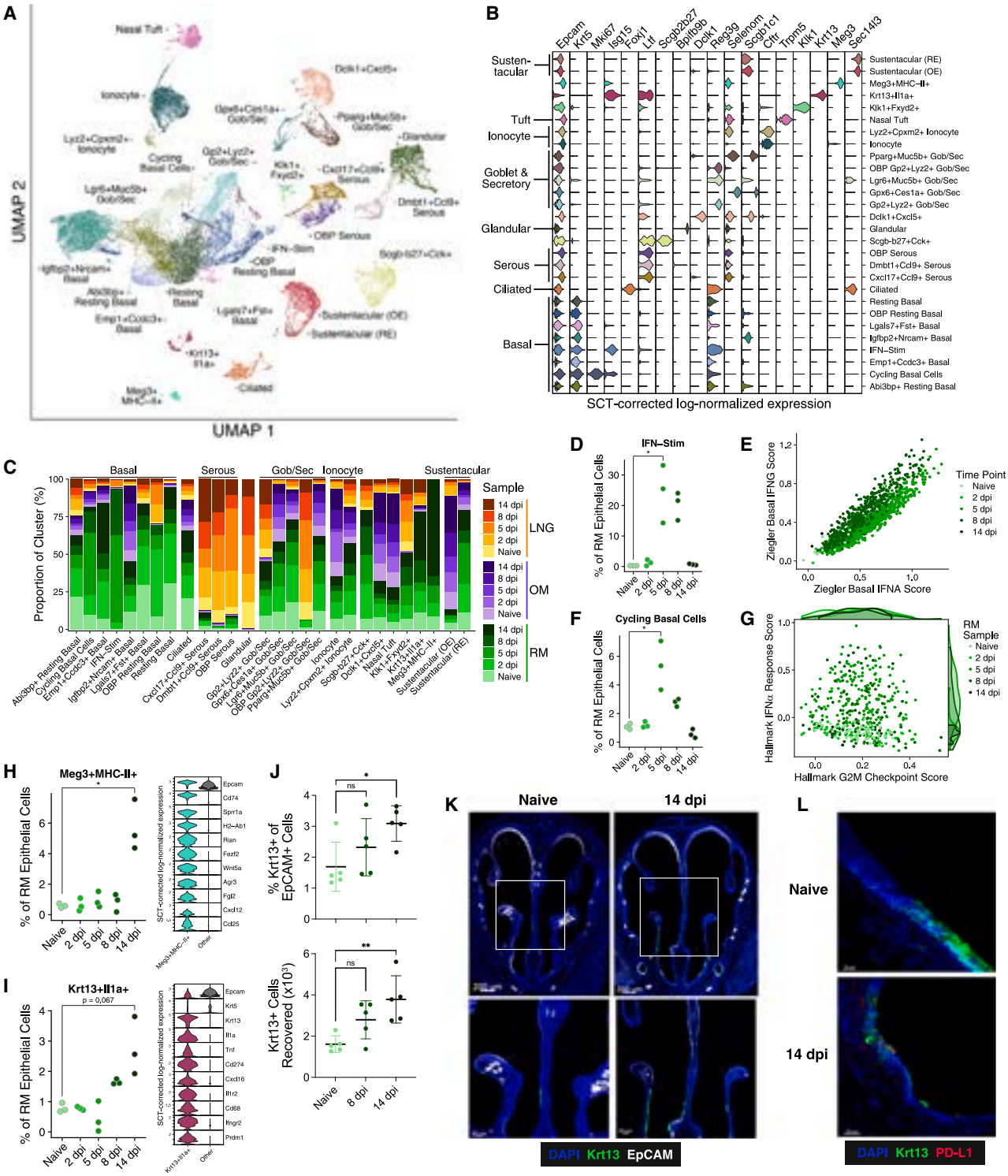

Figure 3. Epithelial cell subclustering reveals diverse subsets, including transient IFN-responsive/cycling cells and rare cells with immune-interaction potential arising 14 dpi

(A) UMAP embedding of 38,367 epithelial cells across 28 clusters.

(B) Violin plot depicting epithelial lineage and subset marker expression levels across all discovered clusters (see Table S1).

(C) Stacked bar chart depicting the relative proportions of cells annotated for each cluster by region and time point.

(D) Relative frequencies of cells clustered as IFN-Stim as a proportion of all epithelial cells. Welch's t test.

(E) IFN-Stim epithelial cell scores for signatures derived from airway basal cell cultures stimulated with IFNα or IFNγ (Ziegler et al.[52]).

(legend continued on next page)

Please cite this article in press as: Kazer et al., Primary nasal influenza infection rewires tissue-scale memory response dynamics, Immunity (2024), https://doi.org/10.1016/j.immuni.2024.06.005

order across PC1-2 (Figure 2F), suggesting that dynamic and linked responses occur over the course of infection in this region. PCA loadings highlight a shift from resting basal cells, fibroblasts, and ciliated cells in naive mice and 2 dpi to diverse activated myeloid and lymphoid clusters 5 and 8 dpi that gave way to specific goblet/secretory cells, T_{RM}-like cells, and mature myeloid cells following viral resolution 14 dpi (Figure 2G). Even though virus was cleared by 14 dpi, all three nasal regions reached compositions distinct from naive mice at this time point.

Regional epithelial diversity in the nasal mucosa dynamically changes during IAV infection

We next evaluated epithelial cell responses to IAV infection. Subclustering on all epithelial cells yielded 28 clusters encompassing diverse differentiation states and functions (Figures 3A, 3B, and S3A; Table S1). In addition to known subsets (e.g., goblet, basal, etc.), we identified unique clusters of epithelial cells potentially specific to the nasal mucosa and present in steady-state and infection that separated in UMAP space: *Scgb-b27*$^+$*Cck*$^+$, *Klk1*$^+$ *Fxyd2*$^+$, *Meg3*$^+$*MHC-II*$^+$, and *Krt13*$^+$*Il1a*$^+$ cells. Comparison with human nasal biopsy and swab datasets,[10,49] readily annotated known epithelial subsets and suggested that the *Krt13*$^+$*Il1a*$^+$ cluster was squamous-like (Figure S3B). The other unique clusters did not map reliably to human subsets, potentially due to limitations in sampling human tissue. Epithelial clusters were unevenly distributed across regions (Figure 3C): nasal tuft cells, ionocytes, *Dclk1*$^+$ cells,[50] and olfactory sensory neuron supportive sustentacular cells[51] were enriched in OM, whereas serous and glandular cells were specific to LNG.

To understand how IAV infection impacts nasal epithelial cells, we determined which clusters harbored viral reads. The distribution of IAV UMIs across all epithelial clusters showed that IAV+ cells were enriched in the IFN-stimulated cluster, followed by cycling basal and ciliated cells (Figure S3C). The IFN-stimulated cluster, largely restricted to the RM, expressed *Krt5*, a basal cell marker, together with *Cxcl17*. Comparing cells within the IFN-stimulated cluster by presence of IAV transcripts, IAV+ cells showed relatively higher levels of ISGs but lower expression of transcription factors *Atf3*, *Egr1*, and *Junb* (Figure S3D). Although infection was well-established at 2 dpi, IFN-stimulated epithelial cells only arose at 5 dpi and composed ~20% of all RM epithelial cells 5 and 8 dpi (Figure 3D). The substantial detection of IAV transcripts by bulk RNA-seq (Figure S2E), but lack of an IFN-response signature in total RM tissue at 2 dpi (Figure 2H), suggests that besides selective loss of IAV+ cells during processing, host silencing mechanisms by IAV may also contribute to the muted IFN response.[53] To understand the relative contribution of different IFNs to the IFN-stimulated epithelial cluster, we scored these cells with gene lists derived from nasal basal cells stimulated with IFNα or IFNγ *in vitro*.[52] Although IFNα and IFNγ induce partially overlapping ISGs, cells 5 dpi scored higher for the IFNα signature and cells 8 dpi scored higher for the IFNγ signature (Figures 3E and S3E).

Cycling basal cells demonstrated a similar transient increase in abundance, peaking 5 dpi (Figure 3F). Many ISGs were significantly increased at this time point (Figure S3F). Given that the epithelial IFN response can impede proliferation and tissue repair in the lower airway,[54,55] we assessed whether individual nasal basal cells co-express pathways for cell cycle and IFN response. Gene set analysis confirmed significant enrichment for both pathways in cycling basal cells; a mutually exclusive apoptosis pathway was also significant (Figure S3G). Pathway module scoring showed that although the IFNα response score changed over time, the G2M checkpoint score was equally distributed across time points and independent of IFNα response (Figure 3G). Thus, unlike their lower respiratory tract counterparts, proliferating nasal basal cells may support concurrent ISG expression during primary infection alongside non-proliferative IFN-stimulated basal cells.

The compositional PCA separates RM samples at 14 dpi from other time points (Figure 2G). Among epithelial cells, two clusters, *Emp1*$^+$*Ccdc3*$^+$ basal cells and *Gp2*$^+$*Lyz2*$^+$ goblet/secretory cells, accumulated to 9%–12% of all epithelial cells following viral clearance by 14 dpi (Figure S3H). In addition to *Gp2* and *Lyz2*, the goblet/secretory subset was also enriched for *Il33*, *Muc1*, and *Cd14*, suggesting a shift toward an antibacterial state. Additionally, two rare (~1% of RM epithelial cells) and transcriptionally distinct subsets of epithelial cells—*Meg3*$^+$ MHC-II$^+$ and *Krt13*$^+$*Il1a*$^+$—accumulated at 14 dpi. The *Meg3*$^+$ MHC-II$^+$ subset highly expressed maternally imprinted Meg genes (*Meg3*, *Rian*) alongside *Cd74*, H2 class II genes, *Wnt5a*, *Cxcl12*, and *Ccl25* (Figure 3H). They also uniquely expressed *Fezf2*, a transcription factor connected to thymic self-antigen expression and immune tolerance induction by thymic epithelial cells.[56]

The *Krt13*$^+$*Il1a*$^+$ subset uniquely expressed *Krt13*, a keratin described on hillock cells in the mouse trachea[57,58] and squamous/suprabasal cells in the human nasal turbinate.[49] These *Krt13*$^+$*Il1a*$^+$ cells exhibited several markers specific to tracheal hillock cells, including *Lgals3*, *Ecm1*, and *Anxa1*, but were not enriched for *Cldn3* or club cell marker *Scgb1a1*. Unlike hillock cells, this nasal subset expressed genes for several secreted and membrane-bound immune cell regulatory factors, including *Il1a*, *Tnf*, *Cd274* (PD-L1), *Ifngr2*, and *Cxcl16*, as well as secretory proteins like *Defb1*, *Muc4*, and *Muc1* (Figure 3I). Flow cytometry confirmed Krt13$^+$ cell accumulation 14 dpi (Figure 3J). Given the potential for these *Krt13*$^+$ cells to communicate with immune cells, we stained for Krt13 to understand their distribution

(F) Same as in (D) for the cycling basal cell cluster.
(G) Scatterplot of gene module scores for the Hallmark IFNα response and Hallmark G2M checkpoint gene lists (MsigDB v7.5.1) in cycling basal cells. Density plots represent the scatterplot data.
(H and I) Relative frequency plots of *Meg3*+MHC-II+ (H) and *Krt13+Il1a*+ (KNIIFE cells, I) clusters as a proportion of all epithelial cells per replicate RM sample. Violin plots of select cluster specific/enriched genes, except for *Epcam* and *Krt5* (FDR corrected p values $\leq 10^{-242}$, 1-vs.-rest Wilcoxon rank sum test).
(J) Frequencies of Krt13+ epithelial cells by flow cytometry (n = 5/time point). Kruskal-Wallis test; mean with standard deviation.
(K) Representative immunofluorescence images of the anterior nasal mucosa in naive mice (left) and 14 dpi (right) staining for Krt13 (green) and EpCAM (white).
(L) Representative images within the region shown in (K) in naive mice (top) and 14 dpi (bottom) staining for Krt13 (green) and PD-L1 (red). Welch's t test. $^*p < 0.05$, $^{**}p < 0.01$.

Please cite this article in press as: Kazer et al., Primary nasal influenza infection rewires tissue-scale memory response dynamics, Immunity (2024), https://doi.org/10.1016/j.immuni.2024.06.005

throughout the nasal cavity. The strongest signal for Krt13 was along the nasal floor in the anterior RM (Figure 3K) and, more distally, where the nasal mucosa meets the oral mucosa (Figure S3I). Comparing samples from naive mice and those 14 dpi, we saw increased Krt13 staining and co-localization with PD-L1 in the post-infection samples (Figure 3L). Thus, following resolution of IAV infection, rare subsets of nasal epithelial cells with immune communication potential accumulate in the RM.

Neutrophils mature and activate in the RM immediately following IAV infection

Given the relationship between increased neutrophil activation in the nose prior to RSV infection and higher symptom occurrence,[13] and the large number of granulocytes captured (n = 7,987), we investigated the transcriptional programs and changes in frequency in our dataset. Subclustering and UMAP embedding revealed a continuum of neutrophil development and cluster of mast cells (Figures 4A and S4A; Table S1). Many neutrophils originated from OM samples (Figures 2B and S4B) and are likely present in high numbers in the bone marrow.[42] Pseudotime analysis across the OM and RM recapitulated known maturation gene expression patterns in the blood[59] and systemically[60] (Figures 4B, 4C, and S4C). Precursors and immature neutrophils present largely in OM samples, likely in bone marrow, may differentiate into activated and mature subsets in RM that accumulate in high frequencies during infection.

By 2 dpi, neutrophil composition in the RM transitioned into mature IFN-stimulated and MHC-I^{hi} states alongside an antimicrobial immature subset near the end of the pseudotime development trajectory (Figure 4D). Neutrophil accumulation is one of the earliest changes in the RM following infection and may constitute some of the earliest responses to local viral molecules and/or type-I IFN. The OM exhibited increased frequencies of mast cells, progenitors, and cycling immature granulocytes in 2-out-of-3 mice at 5 dpi, likely within the bone marrow, indicating IAV infection may induce changes to adjacent hematopoiesis (Figure S4D). Thus, using our sampling strategy, neutrophil activation and maturation mark the earliest detectable responses in the nasal mucosa to IAV infection.

Stepwise recruitment of monocytes and differentiation of MDMs

Next, we explored heterogeneity among non-granulocyte myeloid cells (Figures 4E and S4E; Table S1), annotating a spectrum of macrophages, monocytes, and dendritic cells (DCs). Most myeloid clusters were present in all nasal regions, with some exceptions like IFN-stimulated monocytes and MDMs, which were restricted to the RM (Figure S4F). Although non-existent at baseline, 30%–40% of all myeloid cells belonged to antiviral monocyte and MDM clusters 5 and 8 dpi, respectively (Figure 4F). The accumulation of monocytes and MDMs is concordant with lower frequencies of several tissue macrophage clusters, likely reflecting an overall increase in the total number of myeloid cells in the tissue as monocytes infiltrate from circulation.

To understand the difference between the IFN-stimulated monocytes and MDMs, we performed differential expression analysis between clusters (Figure 4G). Although monocytes had higher ISG expression than MDMs, compared with resting tissue macrophages, the MDMs still expressed ISGs at high levels. IFN-stimulated MDMs expressed more *Cxcl9* and *Cxcl16*, whose receptors (CXCR3 and CXCR6, respectively) support T_{RM} cell development in the lung.[61,62] Comparison of response scores to IFNα and IFNγ stimulation, derived from *in vitro* macrophage cultures[63] on all IFN-stimulated monocytes and MDMs, showed relatively higher expression of the IFNα score at 5 dpi and the IFNγ score at 8 dpi (Figures S4G and S4H), similar to IFN-stimulated epithelial cells (Figure 3E).

The IFN-stimulated MDM cluster had the largest number of IAV+ cells of all myeloid cells (Figure S4I). Bystander analysis revealed higher expression of some ISGs (*Isg15*, *Ifit3*, and *Rsad2*) in IAV+ myeloid cells, like IAV+ epithelial cells (Figure S4J). However, the small fraction of IAV+ cells, compared with their bystander counterparts, had lower expression of MHC-II genes and other ISGs, including *Ccl6* and *Cxcl9*, suggesting reduced antigen presentation and immune cell recruitment capacity. This is consistent with prior research in the lung showing that IAV suppresses myeloid cell activation and maturation.[64,65]

The rapid shift in the myeloid compartment from IFN-stimulated monocytes at 5 dpi to a predominance of IFN-stimulated MDMs 8 dpi (Figure 4F) suggested that recruited monocytes differentiated into MDMs within the RM during this interval. To test this, we treated mice with an anti-CCR2 antibody to deplete circulating monocytes from the blood for 48 h[66,67] (Figure S4K). In the nasal mucosa, we stained for patrolling (Ly6C$^+$) differentiating monocytes, which increase MHC-II, F4/80, and CD64 expression as they differentiate into MDMs (Figure S4L). To deplete monocytes during recruitment to the nasal mucosa (between 3 and 7 dpi), we treated animals with anti-CCR2 from 3 to 5 dpi. Depletion led to reduced frequencies of patrolling monocytes at 8 dpi (Figure 4H). Moreover, the proportion and number of MHC-II$^+$ cells (i.e., differentiating MDMs) were considerably lower, suggesting that the large proportion of IFN-stimulated MDMs measured at 8 dpi by scRNA-seq are derived from monocytes. Together, these data show that IAV infection induces a large recruitment of antiviral monocytes 5 dpi that differentiate into MDMs by 8 dpi in the RM.

Antiviral NK cell responses precede transient effector T cells that are replaced by durable T_{RM}-like cells

Following the accumulation of inflammatory monocytes and MDMs at 5 and 8 dpi, we anticipated a strong lymphocyte response during IAV infection. We next investigated NK and T cells, which are essential in clearing IAV infection in the lungs[68] and nasal mucosa.[21] We captured diverse innate lymphoid cells (NK, ILCs), $\gamma\delta$T cells, and several clusters of $\alpha\beta$T cells (Figures 5A and S5A; Table S1). Most T and NK cell clusters were enriched or restricted to the RM, but *Ccr7*$^+$ CD8$^+$ T cells, ILCs, and $\gamma\delta$T cells were also found in the OM and LNG (Figure S5B). By frequency, IFN-stimulated T and NK cells accumulated 5 dpi alongside cytotoxic NK cells that remained elevated through 8 dpi (Figure 5B). At 8 dpi, the IFN responses shifted to effector antiviral T cell subsets, with high abundances of *Gzmk*$^+$ CD8$^+$, Th1-like *Ifng*$^+$*Cd200*$^+$ CD4$^+$, cycling, and Helios$^+$ T cell clusters (Figure 5C). These effector responses were short-lived, however,

Please cite this article in press as: Kazer et al., Primary nasal influenza infection rewires tissue-scale memory response dynamics, Immunity (2024), https://doi.org/10.1016/j.immuni.2024.06.005

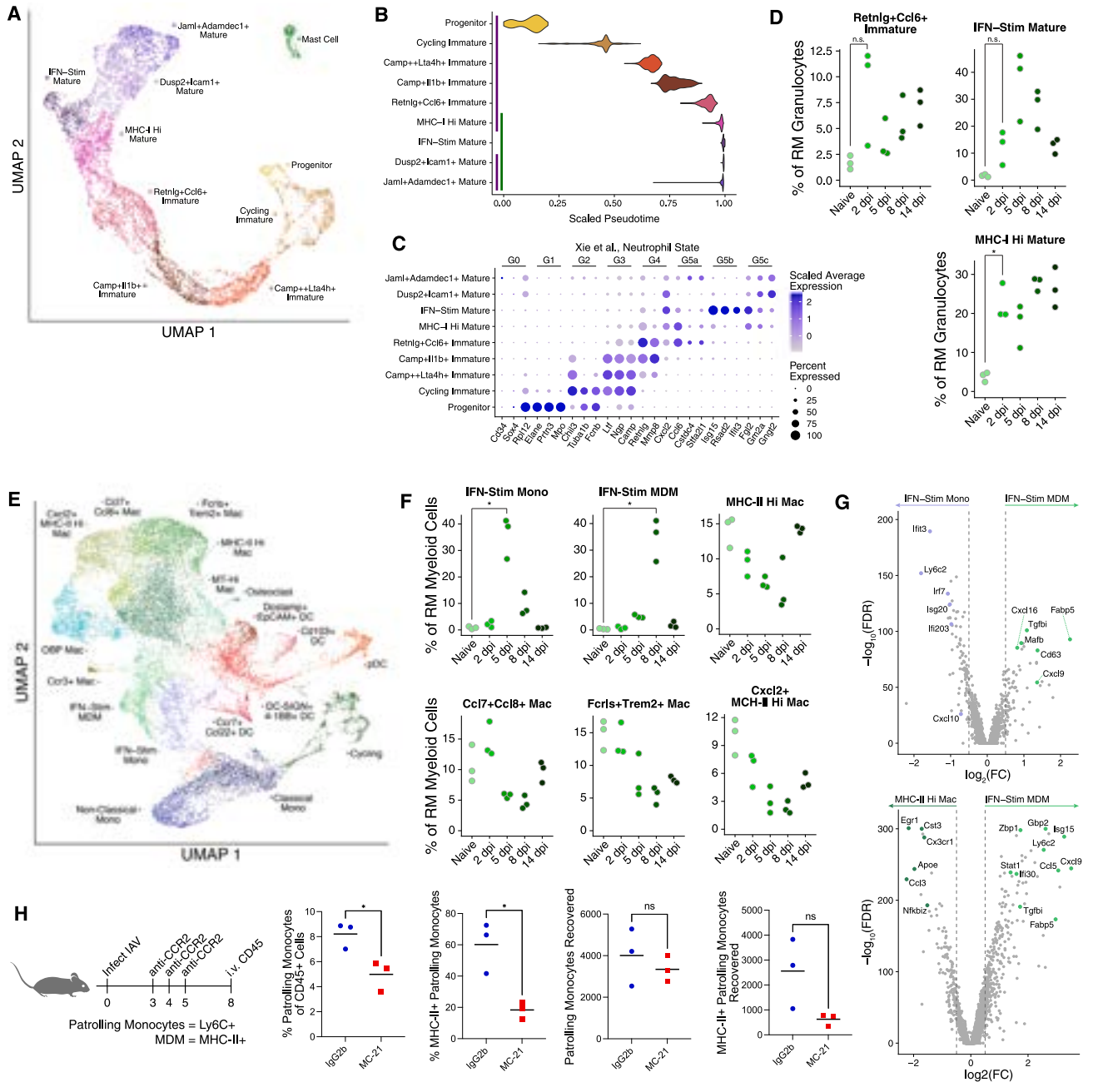

Figure 4. Immediate neutrophil responses are bolstered by recruited antiviral monocytes that differentiate into monocyte-derived macrophages

(A) UMAP embedding of 7,987 granulocytes across 10 clusters.

(B) Violin plot of assigned pseudotime values to all neutrophils split by cluster identity. Purple (OM) and green (RM) bars depict in which regions each cluster can be found at high frequencies (see Figure S4B).

(C) Average expression of blood neutrophil development genes annotated in Xie et al.[60]

(D) Relative frequencies of various neutrophil clusters as a proportion of all granulocytes per replicate RM sample. Welch's t test.

(E) UMAP embedding of 22,654 macrophages, monocytes, and dendritic cells (DCs) across 17 clusters.

(F) Relative frequencies of various myeloid cell clusters as a proportion of myeloid cells. Welch's t test.

(G) Volcano plots depicting differentially expressed genes ($|\log_2 FC| \geq 0.5$; FDR < 0.01) between IFN-Stim MDMs and IFN-Stim Mono (top) and MHC-II-Hi Macs (bottom). Only cells from RM were used. Genes of interest are labeled.

(H) Mice were infected with IAV and treated daily 3–5 dpi with either MC-21 (anti-CCR2; $n = 3$) or IgG2b (isotype control; $n = 3$). Patrolling monocytes were distinguished from circulating monocytes based on lower expression of Ly6C. Flow cytometry statistics are gated on CD45-EV+ cells; Welch's t test, $^*p < 0.05$.

Please cite this article in press as: Kazer et al., Primary nasal influenza infection rewires tissue-scale memory response dynamics, Immunity (2024), https://doi.org/10.1016/j.immuni.2024.06.005

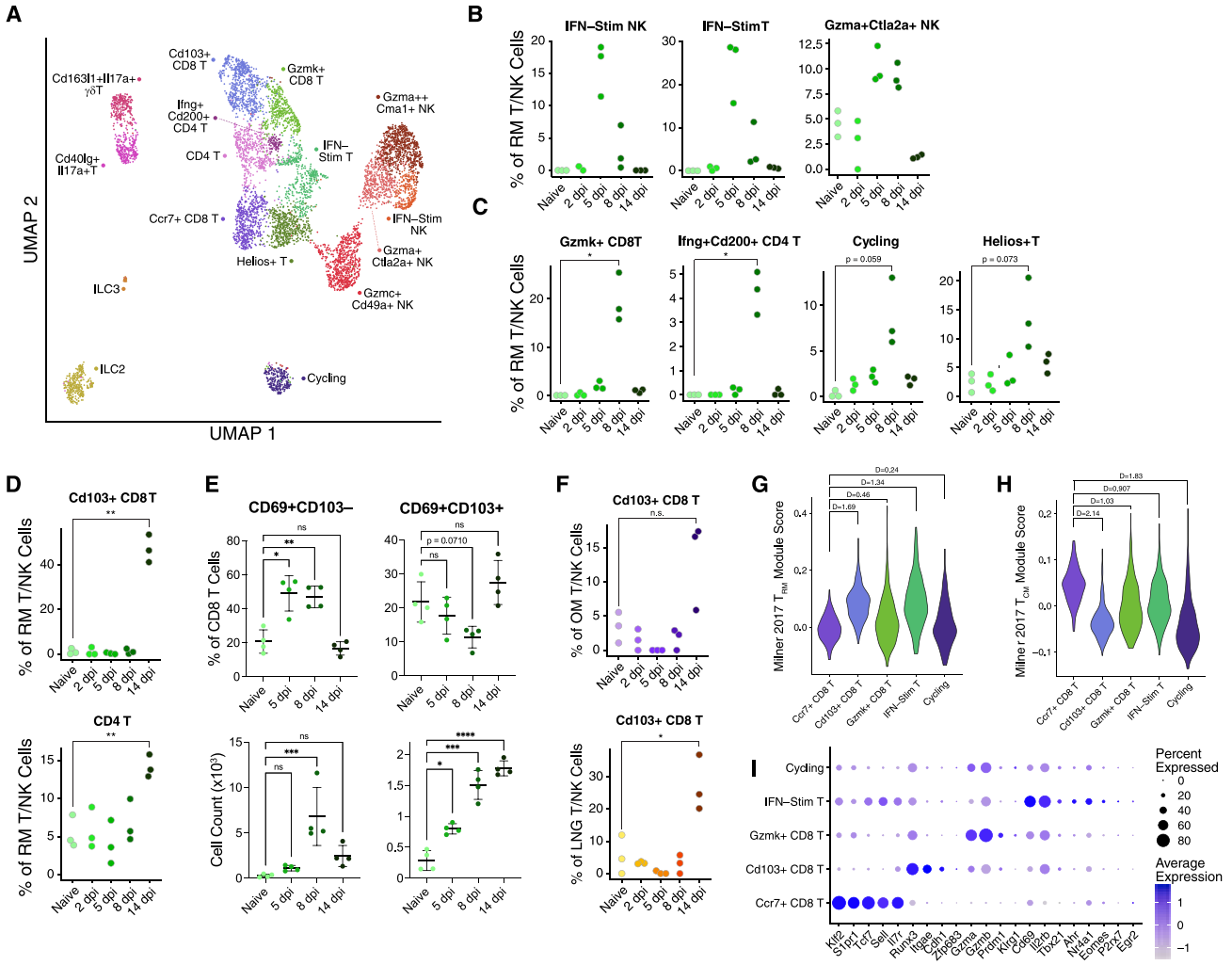

Figure 5. Effector CD4 and CD8 T cells 8 dpi are replaced by T_{RM} cells following viral clearance

(A) UMAP embedding of 6,573 T, NK, and innate lymphoid cells across 16 clusters.

(B–D) Relative frequencies of various clusters as a proportion of all T and NK cells. Welch's t test.

(E) Mice were infected with 10^4 pfu IAV PR8 and RM tissue was collected to stain for T cells. Kruskal-Wallis, mean with standard deviation

(F) Relative frequencies of Cd103+ CD8 T cells per OM and LNG sample replicates. Welch's t test.

(G and H) Violin plots depicting gene module score derived from the universal T_{RM} signature (G) and central memory signature (H), as published in Milner et al.,[70] across all CD8 T cell clusters in RM. Cohen's D for effect size is reported between *Ccr7*+ CD8 T cells and each other cluster.

(I) Dotplot of genes encoding for canonical surface markers, proteases, and transcription factors enriched or absent in T_{RM} cells from circulating memory and naive CD8 T cells. Gene list derived from Crowl et al.[71] $^*p < 0.05$, $^{**}p < 0.01$.

followed by T_{RM}-like cells and resting $CD4^+$ T cells (Figure 5D). Flow cytometry of RM tissue at matched time points confirmed an influx of $CD69^+CD103^-$-activated $CD8^+$ T cells at 5 and 8 dpi that diminished by 14 dpi alongside the accumulation of $CD69^+CD103^+$ T_{RM}-like cells (Figure 5E). Although detectable infection was largely restricted to the RM, T_{RM} cells also increased in OM and LNG 14 dpi (Figure 5F), suggesting that even low levels of infection can result in T_{RM} accumulation.[69] Examination of two published T_{RM} signatures[70,71] confirmed that our $Cd103^+$ $CD8^+$ T cell cluster resembled bona fide T_{RM} cells in other tissues, scoring highest for a pan-tissue signature (Figures 5G and 5H), with higher expression of *Runx3* and low levels of *Tcf7* and *Klf2* (Figure 5I). In summary, effector T cell responses in the RM 8 dpi are replaced by T_{RM}-like cells across all nasal mucosa regions following viral clearance.

IgA^+ cells populate the nasal mucosa following viral clearance

Following IAV infection, local mucosal plasma cells and activated B cells secrete neutralizing soluble IgA into the airways.[24,72,73] In the lungs, resident memory B cells form after primary infection and can be recruited upon secondary challenge to produce additional antibodies,[74] suggesting infection can lead to long-term changes in both local and distal B cell subsets. We identified clusters of naive and developing B cells (primarily in OM) and a rare cluster of IgG^+/IgA^+ early plasmablasts

Please cite this article in press as: Kazer et al., Primary nasal influenza infection rewires tissue-scale memory response dynamics, Immunity (2024), https://doi.org/10.1016/j.immuni.2024.06.005

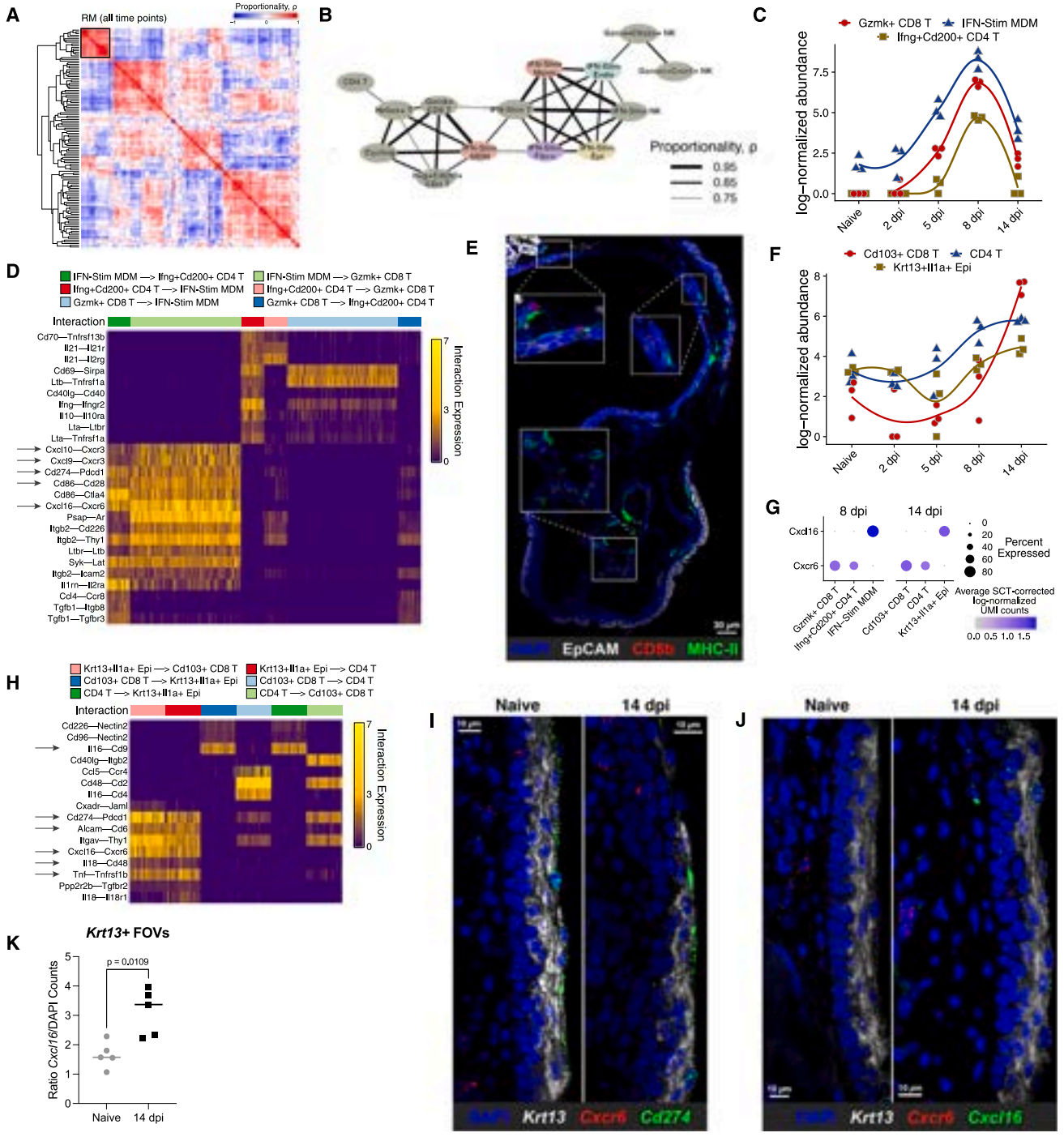

Figure 6. Proportionality and cell-cell communication analyses highlight the CXCR6-CXCL16 signaling pathway in T cell:MDM and T cell:KNIIFE cell interactions

(A) Hierarchically clustered similarity heatmap of sample replicate proportionality calculated across all RM primary infection time points. Black box highlights the proportionality results for the cell clusters depicted in (B).

(B) Network of significantly proportional (FDR < 0.01) cell clusters as in (A). Nodes are colored by cell type and edge weight is representative of proportionality.

(C) Abundance plot of *Gzmk*+ CD8 T cells, IFN-Stim MDMs, and Ifng+Cd200+ CD4 T cells in replicate RM samples. Smoothed lines are calculated using local polynomial regression fitting.

(D) Heatmap depicting a subset of differentially expressed receptor-ligand interaction pairs between single-cell pairs identified by NICHES[77] for the clusters depicted in (C); see Table S3. Arrows highlight interactions described in the text.

(E) Representative immunofluorescence imaging of maxillary turbinate at 8 dpi staining for EpCAM (gray), Cd8b (red), and MHC-II (green). White boxes show enlarged insets.

(legend continued on next page)

Please cite this article in press as: Kazer et al., Primary nasal influenza infection rewires tissue-scale memory response dynamics, Immunity (2024), https://doi.org/10.1016/j.immuni.2024.06.005

(Figures S5C and S5D; Table S1). The preponderance of precursor and developing B cell subsets in OM likely reflects bone marrow cells. IgG$^+$/IgA$^+$ plasmablasts were found at highest frequency within LNG tissue (Figure S5E).

Pro-B and pre-B cells collectively comprised up to 80%–90% of all B cells in the OM 5 dpi, increasing from 5%–15% at baseline, suggesting that IAV infection may induce local B cell proliferation and differentiation in the bone marrow following infection and/or egress of mature B cells from this region (Figure S5F). This increase in B cell precursor frequency paralleled that of granulocyte precursors (Figure S4D), supporting the notion of activation in nasal bone marrow. By 14 dpi, IgG$^+$/IgA$^+$ early plasmablasts were consistently detected in the RM, but their recovery was variable in OM and LNG, potentially due to biological variability and/or inconsistent cell capture. Flow cytometry staining for intracellular IgA confirmed the increase of IgA$^+$ cells in both RM and LNG (Figure S5G) at 14 dpi. Moreover, imaging of the RM and LNG at 30 dpi confirmed the presence of IgA$^+$ cells in both regions following infection (Figure S5H). Thus, B cells may undergo proliferative development during acute IAV infection and IgA$^+$ cells accumulate in the RM and LNG following clearance.

Proportionality guided cell-cell communication analysis highlights the CXCL16-CXCR6 signaling axis in T cell responses

To understand how compositional changes during primary infection may be coordinated across multiple cell subsets, we characterized relationships between pairs of cell clusters over time. We employed proportionality analysis,[75] an alternative to correlation that avoids the intra-sample dependence present in compositional data,[76] to find cell clusters with similar abundance trajectories in the RM (STAR Methods). We discovered a highly structured proportionality landscape with 101 significantly proportional cluster pairs (false discovery rate [FDR] < 0.05) (Figures 6A and S6A). To understand coordination among larger groups of cell clusters, we built a network of all proportional cluster pairs (Figure S6B). The network revealed larger groups made up of clusters from several different cell types and smaller and single-pair groups with 1–2 contributing cell types. To characterize coordination among diverse immune and epithelial cell clusters, we investigated groups of clusters with high proportionalities.

The strongest proportionality was observed among highly networked IFN-stimulated clusters and effector T cell clusters (Figure 6B). Given the large myeloid and T cell responses 8 dpi and the possibility that activated MDMs may function as antigen presenting cells alongside DCs, we focused on the relationship between the IFN-stimulated MDM, *Gzmk*$^+$ CD8$^+$ T cell, and *Ifng*$^{+-}$ *Cd200*$^+$ CD4$^+$ T cell clusters. Plotting abundance values confirmed synchronous trajectories with transient accumulation starting 5 dpi, peaking 8 dpi, and waning 14 dpi (Figure 6C). We next assessed cell-cell communication potential using NICHES, an approach that finds single-cell pairs with multiplicative high expression of known interacting ligands and receptors.[77] Differential ligand-receptor expression between groups of cell pairs was then used to identify interactions specific to pairs of clusters (STAR Methods and Table S3). Applied to cells from these three clusters at 8 dpi, we found several predicted, literature-supported interactions between the MDM cluster and both effector T cell clusters, including *Cd274-Pdcd1* (PD-L1-PD-1), *Cd86-Cd28*, *Cxcl9/10-Cxcr3*, and *Cxcl16-Cxcr6* (Figure 6D). Imaging confirmed the spatial proximity of RM CD8$^+$ T cells and MDMs/DCs 8 dpi (Figure 6E).

The second-largest network included various myeloid, granulocyte, and epithelial cell clusters. Intrigued by the inclusion of the late-arising *Gp2*$^+$*Lyz2*$^+$ goblet/secretory cell cluster (Figure S3G), we further investigated this cluster and the two clusters most proportional with it: Cd103$^+$ DCs and *Dusp2*$^+$*Icam1*$^+$ mature neutrophils. Plotting cluster abundances confirmed that all three clusters peaked following viral clearance 14 dpi (Figure S6C). Closer inspection of differentially expressed ligand-receptor pairs revealed potential pro-inflammatory signaling by *Gp2*$^+$*Lyz2*$^+$ Gob/Sec cells to mature neutrophils via *Sftpd-Sirpa*, which blocks CD47 binding,[78] *Cirbp-Trem1*, which occurs in sepsis,[79] and *Tgfb2-Tgfbr1*. DC-neutrophil interactions included *Ccl2-Ccr1* and *Il18-Il18rap*, suggesting mutual immune recruitment/homeostasis (Figure S6D). These interactions suggest that late-arising *Gp2*$^+$*Lyz2*$^+$ goblet/secretory cells may recruit and regulate Cd103$^+$ DCs and mature neutrophils in the RM following viral clearance.

Like IFN-stimulated MDMs producing *Cxcl16* 8 dpi in concert with abundant *Cxcr6* expressing effector CD8$^+$ and CD4$^+$ T cells, *Krt13*$^+$*Il1a*$^+$ epithelial cells expressing *Cxcl16* increased alongside *Cxcr6*$^+$ T_{RM}-like and CD4$^+$ T cells 14 dpi (Figures 6F and 6G). Although not significantly proportional, we applied cell-cell communication analysis to cells from 14 dpi in these three clusters, given the role of CXCL16-CXCR6 signaling in T_{RM} localization in the lower airways.[62,80] In addition to annotating the *Cxcl16-Cxcr6* interaction, the analysis captured additional interactions like *Cd274-Pdcd1*, *Tnf-Tnfsrsf1b*, *Il18-Cd48*, *Alcam-Cd6*, and *Il16-Cd9* (Figure 6H). RNAscope of nasal floor in a naive mouse and 14 dpi confirmed expression of *Cd274* (PD-L1) and *Cxcl16* by *Krt13*+ cells in the vicinity of cells expressing *Cxcr6* (Figures 6I and 6J). Comparison between time points showed higher relative abundance of *Cxcl16* transcripts within *Krt13*$^+$ regions at 14 dpi compared with naive (Figures 6K and S6E). Considering the transcriptional programming and localization of these cells, we propose the name *Krt13*+ nasal

(F) Abundance plot of Cd103+ CD8 T cells, CD4 T cells, and *Krt13+Il1a+* epithelial (KNIIFE) cells in replicate RM samples.
(G) Dotplot of *Cxcl16* and *Cxcr6* expression 8 dpi (left) in the clusters depicted in (C) and 14 dpi (right) in the clusters depicted in (F).
(H) Heatmap like (D) for the clusters shown in (F).
(I) Representative RNAscope in situ staining for *Krt13* (gray), *Cxcr6* (red), and *Cd274* (i.e., PD-L1; green) of the nasal floor in a naive mouse and 14 dpi mouse. Images depict a maximal intensity projection across 5 μm (10 slices) in the z plane.
(J) RNAscope as in (I) staining with *Krt13* (gray), *Cxcl6* (red), *and Cxcl16* (green).
(K) Quantification of co-localization of *Krt13* and *Cxcl16* RNAs across multiple RNAscope images from the nasal floor (n = 5/time point). Ratio of the number of *Cxcl16* spots per nucleus within each *Krt13+* region is reported. Welch's t test, *p < 0.05.

Please cite this article in press as: Kazer et al., Primary nasal influenza infection rewires tissue-scale memory response dynamics, Immunity (2024), https://doi.org/10.1016/j.immuni.2024.06.005

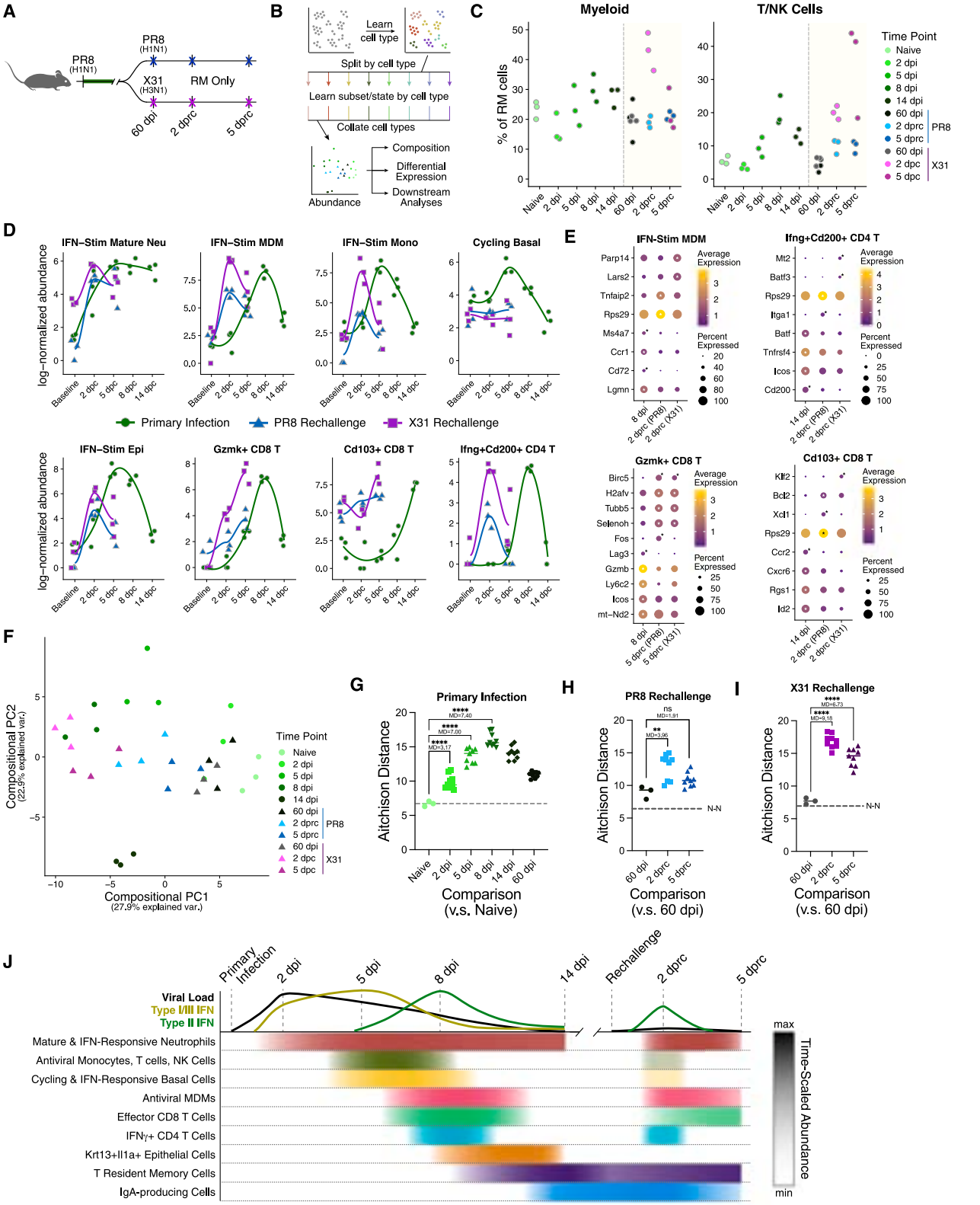

Figure 7. IAV rechallenge induces accelerated and coordinated memory immune responses

(A) Experimental design for IAV rechallenge experiments. Dprc, days post rechallenge.

(B) Analysis scheme applied to RM samples to learn cell cluster identity.

(legend continued on next page)

Please cite this article in press as: Kazer et al., Primary nasal influenza infection rewires tissue-scale memory response dynamics, Immunity (2024), https://doi.org/10.1016/j.immuni.2024.06.005

immune-interacting floor epithelial (“KNIIFE”) cells. KNIIFE cells are a fraction of cells on the nasal floor expressing *Cxcl16* at 14 dpi alongside myeloid cells, suggesting that this region of the nasal mucosa may be important in instructing T_{RM} cells following viral clearance and/or tissue damage.

In summary, proportionality analysis coupled with cell-cell communication approaches reveal temporally synced cell cluster abundance changes over the course of primary infection and highlight potential cell-cell interactions contributing to T cell function and residual inflammation following viral clearance.

IAV rechallenge is characterized by accelerated and concurrent myeloid and lymphocyte memory responses

Having developed a tissue-scale response timeline of acute IAV infection in the nasal mucosa, we next asked how strain matched and unmatched induced memory responses differ from primary infection. After priming mice with IAV PR8 infection, we rechallenged 60 dpi with either PR8 or IAV X31, a H3N2 strain (Figure 7A). In the PR8→PR8 arm, both antibody- and T cell-mediated mechanisms of protection will occur; in the PR8→X31 arm, antibodies from the primary infection will fail to neutralize IAV but T cells will exhibit memory responses.[21] Sampling RM prior to rechallenge at 60 dpi, and 2- and 5-days-post rechallenge (dprc), we applied a cross-validated label transfer approach using the primary infection data as a reference (Figures S7A–S7C and STAR Methods) to annotate an additional 76,159 cells with labels derived from primary infection (Figure 7B). All cell types present in the primary infection dataset were captured in rechallenge samples and UMAP projection showed overlap between the datasets (Figures S7D and S7E). Plaque assays following PR8 rechallenge detected infectious virus in 1/5 mice in nasal mucosa and 0/5 mice in lung at 2 dprc, and 0/6 in both tissues at 5 dprc, suggesting immediate control of infection or baseline resistance (Figure S7F).

Inspection of cell type frequencies revealed accumulation of immune cells after homologous or heterologous rechallenge. Even with neutralizing antibodies and undetectable viral titers, we measured increased proportions of granulocytes, T & NK cells, and B cells following PR8 rechallenge (Figures 7C and S7G). Following X31 challenge, T & NK cell frequencies increased even higher alongside a substantial but transient accumulation of myeloid cells, supporting a bigger role for T cell-mediated responses in the absence of antibodies. Re-clustering B cells with rechallenge data revealed plasma cells restricted to memory time points (Figures S7H and S7I).

Following annotation, we compared changes in cluster abundances over time between primary and secondary responses to IAV infection (Figures 7D and S7J). Like primary infection, the IFN-stimulated neutrophil subset accumulated immediately and maintained elevated levels through 5 dprc. In homologous rechallenge, IFN-stimulated MDMs rapidly accumulated but monocytes only slightly increased; in heterologous rechallenge, both increased substantially. Given that the total proportion of myeloid cells in the dataset was similar between 60 dpi, 2, and 5 dprc following PR8, these data suggest that MDMs already inside the RM prior to homologous rechallenge quickly responded. Effector Th1 $CD4^+$ T cells were also elevated 2 dprc, but effector $CD8^+$ T and T_{RM} cells were slower to accumulate. Cycling basal cells showed no change in abundance following rechallenge regardless of rechallenge strain, and the increase in IFN-responsive epithelial cells was also stunted. Both the *Meg3*$^+$*MHC-II*$^+$ subset and KNIIFE cells that arose following viral clearance in primary infection remained at low levels throughout rechallenge. Whether or not their roles are restricted to resolving primary infection, there may be a necessary inflammation threshold for their expansion or they may take longer to increase in frequency than the time points sampled. In summary, both PR8 and X31 rechallenge induced the rapid accumulation of several antiviral myeloid and T cell subsets and states despite little detectable virus, with greater induction following heterologous challenge.

We performed differential expression analysis within cell clusters across primary infection, PR8, and X31 rechallenge to assess changes in cell state and found few substantial differences across effector myeloid and T cell subsets (Figure 7E; Table S4).

Although changes in abundance or gene expression on an individual cell subset/state level highlight specific differences between primary and secondary responses, we sought to understand how the collective RM-tissue-scale response changes. Thus, we projected the memory and rechallenge sample replicates into the previously derived compositional PC space for RM in primary infection (Figure 7F). The RM 60 dpi samples separated from naive samples and most resembled 2 dpi, suggesting that even though IAV was cleared by 14 dpi, the nasal mucosa sustained significant changes in composition. For both memory arms, the 2 dprc time point recapitulated the variance described by PC1, with X31 rechallenge samples moving farther negative and overlapping 8 dpi. No significant shift along PC2 suggests that enhanced effector immune responses occur upon rechallenge but not broad antiviral activation across all cell types, like those seen 5 dpi (i.e., IFN-stimulated clusters) (Figure 2H). By 5 dprc in the PR8 rechallenge, the tissue had almost returned to “memory baseline” at 60 dpi in PC space, indicating that responses had already largely resolved. However, in the X31 challenge, a high level of immune infiltration was still taking place

(C) Relative frequencies of myeloid cells and T & NK cells as a proportion of all sequenced cells.
(D) Abundance plots showing overlaid primary infection (green) and rechallenge responses, with PR8 in blue and X31 in pink. Baseline refers to samples from naive mice in primary infection and 60 dpi in rechallenge. Dpc, days post challenge. Smoothed lines are calculated using local polynomial regression fitting.
(E) Dotplots depicting select cluster-specific and differentially expressed genes between primary infection and homologous and heterologous rechallenge in IFN-Stim MDMs (top left), Ifng+Cd200+ CD4 T cells (top right), *Gzmk*+ CD8 T cells (bottom left), and Cd103+ CD8 T cells (bottom right). *FDR < 0.01. See Table S4.
(F) Compositional PCA of primary infection and with secondary challenge RM sample replicates projected.
(G–I) Aitchison distances between sample replicates compositions. (G) All pairs of naive, primary infection, and 60 dpi replicates. (H) 60 dpi with matched PR8 rechallenge replicates. (I) 60 dpi with matched X31 rechallenge replicates. Dotted line plotted shows median naive-naive Aitchison distance (N-N). Multiple hypothesis corrected Welch’s ANOVA. MD, mean difference; *$p < 0.05$; **$p < 0.01$; ***$p < 0.001$, ****$p < 0.0001$.
(J) Timeline schematic of primary IAV infection and homologous rechallenge depicting viral load trajectory, IFN dynamics, and immune and epithelial cell cluster response timing and duration.

Please cite this article in press as: Kazer et al., Primary nasal influenza infection rewires tissue-scale memory response dynamics, Immunity (2024), https://doi.org/10.1016/j.immuni.2024.06.005

at 5 dprc. To assess variation between primary infection and secondary response arms, we re-ran PCA with abundances from all time points, finding some separation between experiments potentially arising from variation in the primary infection (Figure S7K). Nevertheless, infection in the naive setting and both rechallenge paradigms resulted in a concerted and parallel directional shift in compositional PC space, supporting the conclusions of induced effector myeloid and T cell clusters from the projected PCA. PC4 captured the aspects unique to a potentially optimal memory response, with increased abundances of several B cell clusters during homologous rechallenge (Figure S7L).

To quantify the overall difference between time points, we calculated compositional Aitchison distances between all pairs of sample replicates. In primary infection, RM increasingly separated from the naive state up through 8 dpi but then became closer as infection was resolved (Figure 7G). Corroborating the PCA, the nasal mucosa 60 dpi was still distinct from its naive state. Upon rechallenge with PR8, composition also differed from 60 dpi; however, the extent of that difference (MD = 3.96) was less than that between naive and 5 dpi (MD = 7.00) and 8 dpi (MD = 7.40), indicating that the memory response was more succinct (Figure 7H). In comparison, X31 challenge led to the largest distance increase (MD = 9.18), highlighting the massive accumulation of immune cells induced without antibody-mediated protection (Figure 7I). Comparing primary infection time points with peak memory response, each primary infection time point was distinct from 2 dprc, suggesting that prior infection rewires the RM response to IAV infection (Figure S7M). In summary, we present a timeline of the key immune and epithelial cell responses during IAV infection and rechallenge, illustrating that many of the stepwise changes seen in primary infection are more coordinated and accelerated upon rechallenge (Figure 7J).

DISCUSSION

We present a longitudinal, multi-region, scRNA-seq atlas of the murine nasal mucosa during primary and secondary IAV infection. Cataloging the distribution and temporal dynamics of the diverse cell types, subsets, and states present, we develop and apply a compositional framework to understand tissue-scale changes occurring throughout primary and memory responses to viral infection. Infection is characterized by stepwise transient changes in several epithelial and immune subsets in RM associated with viral infection, type I and II IFNs, and viral clearance. By 14 dpi, the tissue has achieved distinct cellular composition from the naive state, with largely only lymphocyte subsets being sustained until 60 dpi. Careful investigation of epithelial cells revealed a rare, unique KNIIFE cell subset and provided evidence for their interaction with *Cxcr6*-expressing lymphocytes on the nasal floor. Employing the primary infection atlas to annotate and interpret rechallenge samples, using both homologous and heterologous IAV strains, showed that rechallenge induces surprisingly widespread yet coordinated changes to cellular composition. We identify accelerated neutrophil, macrophage, and T cell responses in memory with a reduced burden on epithelial cells to express the joint IFN and proliferative response programs of primary infection.

The viral-induced innate signaling and proliferative capacities of epithelium during primary respiratory viral infection associate with disease trajectory.[9,10] In our model, nasal basal cells co-expressed cell-cycle and IFN-response programs at 5 dpi, thought to be non-compatible in lungs.[54,55] Given the diverse roles of nasal epithelial cells and the need to protect olfactory sensory neurons,[81] nasal basal cells may be more tolerant of IFN-response signaling during proliferation than basal cells in the lower airways. Epithelial IFN-induced responses were also reduced upon rechallenge, regardless of IAV strain. This difference could reflect several non-exclusive mechanisms during recall, including reduced or abbreviated IFN production or signaling, lower viral load, or a potential tolerized basal cell state. Airway basal cells can develop transcriptional memory *in vitro*,[82] but whether primary infection confers durable memory to viral immunity, as seen for allergic inflammation,[83] requires further investigation.

Circulating and local myeloid cells can develop trained immunity following primary respiratory viral infection.[39,84–86] After depleting circulating monocytes during acute infection, MDM formation was markedly reduced, indicating that the majority of nasal MDMs at 8 dpi differentiated from newly recruited monocytes. During homologous memory response, MDMs, but not monocytes, increased in abundance 2 dprc despite similar overall myeloid frequencies, suggesting that either recruited MDMs replaced local myeloid cells or MDMs already present in the tissue expanded to exert antiviral effector functions. If the latter, understanding the mechanisms by which enhanced myeloid function is maintained and recalled in the nasal mucosa could yield new avenues for improving mucosal vaccines.[87]

Following viral clearance, unique subsets of epithelial cells with potential immune signaling and inflammatory regulation capacity substantially increased in abundance. We describe one such subset exclusively expressing *Krt13* and *Krt6a* in the nasal mucosa, which we name KNIIFE cells. Structurally, KNIIFE cells were reminiscent of hillock cells in the trachea[57,58] and squamous cells in human nasopharyngeal swabs and biopsies,[10,49] but also expressed several genes often found in macrophages, including *Cd274* (PD-L1), *Ifngr2*, *Tnf*, and *Cxcl16*. This cluster was present at low levels throughout infection until expanding 14 dpi and remaining stable during rechallenge. Our data raise the possibility that KNIIFE cells, by providing a source for CXCL16 beyond that expressed by myeloid cells, may contribute to the establishment and/or maintenance of the T_{RM} cell pool in the nasal mucosa, as suggested in other tissues.[62,80,88–90] The localization of KNIIFE cells prompts the question of whether these cells interact with particles or irritants just entering or settling in the nose and play a regulatory role in tissue tolerance and/or immunity.

Compositional scRNA-seq analyses are becoming more common to discern differences between disease trajectories,[83,91,92] treatment groups,[93,94] and/or species.[95,96] Current tools focus on identifying specific clusters or gene programs that are compositionally distinct between groups.[97–99] However, the power of compositional scRNA-seq data lies in its structure; namely, singular changes in composition cannot be independent and must correspond with mutual changes in other clusters/programs. Leveraging the biological replicates and multiple time points present in our atlas, we utilized straightforward

Please cite this article in press as: Kazer et al., Primary nasal influenza infection rewires tissue-scale memory response dynamics, Immunity (2024), https://doi.org/10.1016/j.immuni.2024.06.005

tools for compositional analysis adapted from microbiome research[76,100,101] to understand tissue-scale changes within the nasal mucosa throughout IAV infection. PCA of clr transformed cell cluster abundances across sample replicates separated nasal regions and depicted structured stepwise changes in epithelial and immune cell subsets throughout infection trajectory. Proportionality analysis, which avoids the spurious associations present in Pearson correlation applied to compositional data,[75] revealed pairs and groups of clusters with significantly similar compositional trajectories (e.g., IFN-stimulated MDMs and effector $CD4^+$ and $CD8^+$ T cells) and can be readily applied to discover similarities across various metadata.

Finally, metrics like Aitchison distance[102] capture holistic changes in tissue-scale cellular composition and support standard tests for differences between group means (e.g., Welch's ANOVA) to assess global similarity and compositional distance traveled by a tissue. Applied to our datasets, the RM "travels" less during an optimal memory response to IAV than during primary infection, suggesting prior infection induces a coordination of previously temporally disparate responses. Heterotypic IAV challenge magnifies these synchronous myeloid and T cell responses, suggesting a compensatory cellular immune mechanism when neutralizing antibodies are ineffective. Together, we propose that these approaches for analyzing scRNA-seq data constitute a framework for understanding and summarizing whole-tissue- and biopsy-scale-changes in cellular composition at high resolution in health, disease, and/or under perturbation.

Collectively, our murine nasal mucosa atlas of primary IAV infection longitudinally catalogs the cell types, subsets, and states present throughout distinct nasal regions. We demonstrate the utility of our dataset to serve as an annotation reference for newly generated scRNA-seq datasets and apply it to understand how the response to infection in the RM differs during memory recall following distinct IAV rechallenges. These findings will help contextualize temporal studies of the nose in humans with more complex exposure histories and highlight key immune and epithelial cell responses to optimize nasal memory responses to future vaccines and therapeutics.

Limitations of the study

We acknowledge that cluster-abundance-based compositional analyses are inherently dependent on how clustering was performed, and thus implicitly incorporate, to some degree, operator bias. Although we believe our approach to be as impartial as possible through use of iterative clustering, robust and reproducible clustering analyses[103–105] could be implemented prior to compositional analysis moving forward. Partial labeling of cells by hashing antibodies may also have obscured changes in composition over time. To our knowledge, this dataset represents the largest scRNA-seq atlas of the murine nasal mucosa to date; however, we may still be under-sampling this complex tissue. Indeed, spatial transcriptomics and/or multiplexed immunofluorescence approaches will help validate the spatial organization and quantification of cell clusters defined here. Although the presence and abundance of KNIIFE cells was confirmed by multiple experimental modalities, the function and impact of these cells on resolving infection and T_{RM} niche formation and maintenance needs further elucidation. We also acknowledge that heterotypic IAV challenge experiments are complex and thus our measured differences in memory responses between PR8 and X31 may be partially dependent on strain derivation and infectious dose, especially given known inherent differences in pathogenicity.[106] Finally additional experiments to test how distinct IFNs, other respiratory pathogens, and vaccination strategies impact the composition and timing of responses in the nasal mucosa to IAV challenge are warranted.

STAR★METHODS

Detailed methods are provided in the online version of this paper and include the following:

- KEY RESOURCES TABLE
- RESOURCE AVAILABILITY
  - Lead contact
  - Materials availability
  - Data and code availability
- EXPERIMENTAL MODEL AND STUDY PARTICIPANT DETAILS
  - Mice
- METHOD DETAILS
  - Virus growth, quantification, and infections
  - Sample processing for single-cell RNA-seq
  - Single-cell RNA-seq
  - Immunofluorescence Microscopy
  - qPCR
  - Antibody-based depletion
  - Flow cytometry
  - RNAscope Microscopy
- QUANTIFICATION AND STATISTICAL ANALYSIS
  - Single-cell RNA-seq pre-processing
  - Clustering, annotation, and IAV+ cell calling
  - Compositional analyses
  - Neutrophil pseudotime analysis
  - Cell-cell signaling analysis
  - RNAscope co-localization quantification
  - Label transfer validation and memory samples

SUPPLEMENTAL INFORMATION

Supplemental information can be found online at https://doi.org/10.1016/j.immuni.2024.06.005.

ACKNOWLEDGMENTS

We thank members of the Ordovas-Montanes and von Andrian labs for insightful discussions and advice. S.W.K. was supported by the Cancer Research Institute's Irvington Postdoctoral Fellowship. J.O.-M. is a New York Stem Cell Foundation—Robertson Investigator. J.O.-M. was supported by the AbbVie-Harvard Medical School Alliance, the Richard and Susan Smith Family Foundation, the AGA Research Foundation's AGA-Takeda Pharmaceuticals Research Scholar Award in IBD—AGA2020-13-01, the HDDC Pilot and Feasibility P30 DK034854, the Leona M. and Harry B. Helmsley Charitable Trust, the Pew Charitable Trusts Biomedical Scholars, the Broad Next Generation Award, the Chan Zuckerberg Initiative Pediatric Networks, the Mathers Foundation, the New York Stem Cell Foundation, NIH R01 HL162642, NIH R01 DE031928, and the Cell Discovery Network, a collaborative funded by the Manton Foundation and the Warren Alpert Foundation at Boston Children's Hospital. This work was supported by the AbbVie-HMS Alliance Program. Sequencing of the scRNA-seq libraries was performed with AbbVie Inc. at the Genomics Research Center and Immunoprofiling Center in collaboration with Steven Leonardo (former AbbVie employee), Abel Suarez-Fueyo, Neha Chaudhary, Jozsef Karman (former AbbVie employee), Aridaman Pandit, and Amlan Biswas. Imaging was performed with MicRoN and HMS Center for Immune Imaging at Harvard Medical School. Anti-CCR2 antibody MC-21 was generously provided by Prof. Matthias Mack (Universität Regensburg). Training for the RNAscope experiments was facilitated by Anoohya N.

Muppirala and Meenakshi Rao at Boston Children's Hospital. Daniel Lingwood (Ragon Institute), Alex Shalek (MIT), Paolo Cadinu, Jeffrey Moffitt (BCH), and Colin Bingle (Sheffield) provided helpful feedback and discussion on experimental design and interpretation of the results. Additionally, we would like to thank Susan Westmoreland for insightful discussions as well as Shankar Subramanian, Michelle Cordoba Gunter, Isabel Chico-Calero, Jochen Salfeld, and Mark Namchuk for supporting the AbbVie-HMS Alliance Program Area 1, which enabled the scope of this work.

AUTHOR CONTRIBUTIONS

Conceptualization, S.W.K., C.M.M., U.H.v.A, and J.O.-M,; methodology, S.W.K., C.M.M., and M.-A.M.; software, S.W.K., E.M.L., and T.J.L.; formal analysis, S.W.K., C.M.M., E.M.L., and T.J.L.; investigation, S.W.K., C.M.M., E.M.L., M.-A.M., E.O., J.M., K.N., and J.O.-M.; data curation, S.W.K.; writing – original draft, S.W.K and C.M.M.; writing – review & editing, S.W.K., C.M.M., E.M.L., U.H.v.A., and J.O.-M.; supervision, U.H.v.A. and J.O.-M.; funding acquisition, S.W.K., U.H.v.A., and J.O.-M.

DECLARATION OF INTERESTS

S.W.K. reports compensation for consulting services with Monopteros Therapeutics, Flagship Pioneering, and Radera Biosciences. J.O.-M. reports compensation for consulting services with Cellarity, Tessel Biosciences, and Radera Biotherapeutics. U.H.v.A. is a paid consultant with financial interests in Avenge Bio, Beam Therapeutics, Bluesphere Bio, Curon, DNAlite, Gate Biosciences, Gentibio, Intergalactic, intrECate Biotherapeutics, Interon, Mallinckrodt Pharmaceuticals, Moderna, Monopteros Biotherapeutics, Morphic Therapeutics, Rubius, Selecta, and SQZ.

Received: May 5, 2023
Revised: March 14, 2024
Accepted: June 10, 2024
Published: July 3, 2024

REFERENCES

1. Harkema, J.R., Carey, S.A., and Wagner, J.G. (2006). The Nose Revisited: A Brief Review of the Comparative Structure, Function, and Toxicologic Pathology of the Nasal Epithelium. Toxicol. Pathol. *34*, 252–269. https://doi.org/10.1080/01926230600713475.
2. Bosch, A.A.T.M., Biesbroek, G., Trzcinski, K., Sanders, E.A.M., and Bogaert, D. (2013). Viral and Bacterial Interactions in the Upper Respiratory Tract. PLoS Pathog. *9*, e1003057. https://doi.org/10.1371/journal.ppat.1003057.
3. Shinya, K., Ebina, M., Yamada, S., Ono, M., Kasai, N., and Kawaoka, Y. (2006). Avian flu: Influenza virus receptors in the human airway. Nature *440*, 435–436. https://doi.org/10.1038/440435a.
4. Roth, G.A., Abate, D., Abate, K.H., Abay, S.M., Abbafati, C., Abbasi, N., Abbastabar, H., Abd-Allah, F., Abdela, J., and Abdelalim, A. (2018). Global, regional, and national age-sex-specific mortality for 282 causes of death in 195 countries and territories, 1980–2017: a systematic analysis for the Global Burden of Disease Study 2017. Lancet *392*, 1736–1788. https://doi.org/10.1016/S0140-6736(18)32203-7.
5. Clark, S.E. (2020). Commensal bacteria in the upper respiratory tract regulate susceptibility to infection. Curr. Opin. Immunol. *66*, 42–49. https://doi.org/10.1016/j.coi.2020.03.010.
6. Park, A., and Iwasaki, A. (2020). Type I and Type III Interferons – Induction, Signaling, Evasion, and Application to Combat COVID-19. Cell Host Microbe *27*, 870–878. https://doi.org/10.1016/j.chom.2020.05.008.
7. Kim, Y.-M., and Shin, E.-C. (2021). Type I and III interferon responses in SARS-CoV-2 infection. Exp. Mol. Med. *53*, 750–760. https://doi.org/10.1038/s12276-021-00592-0.
8. Bastard, P., Zhang, Q., Zhang, S.-Y., Jouanguy, E., and Casanova, J.-L. (2022). Type I interferons and SARS-CoV-2: from cells to organisms. Curr. Opin. Immunol. *74*, 172–182. https://doi.org/10.1016/j.coi.2022.01.003.
9. Sposito, B., Broggi, A., Pandolfi, L., Crotta, S., Clementi, N., Ferrarese, R., Sisti, S., Criscuolo, E., Spreafico, R., Long, J.M., et al. (2021). The interferon landscape along the respiratory tract impacts the severity of COVID-19. Cell *184*, 4953–4968.e16. https://doi.org/10.1016/j.cell.2021.08.016.
10. Ziegler, C.G.K., Miao, V.N., Owings, A.H., Navia, A.W., Tang, Y., Bromley, J.D., Lotfy, P., Sloan, M., Laird, H., Williams, H.B., et al. (2021). Impaired local intrinsic immunity to SARS-CoV-2 infection in severe COVID-19. Cell *184*, 4713–4733.e22. https://doi.org/10.1016/j.cell.2021.07.023.
11. Costa-Martins, A.G., Mane, K., Lindsey, B.B., Ogava, R.L.T., Castro, Í., Jagne, Y.J., Sallah, H.J., Armitage, E.P., Jarju, S., Ahadzie, B., et al. (2021). Prior upregulation of interferon pathways in the nasopharynx impacts viral shedding following live attenuated influenza vaccine challenge in children. Cell Rep. Med. *2*, 100465. https://doi.org/10.1016/j.xcrm.2021.100465.
12. Bastard, P., Rosen, L.B., Zhang, Q., Michailidis, E., Hoffmann, H.-H., Zhang, Y., Dorgham, K., Philippot, Q., Rosain, J., Béziat, V., et al. (2020). Autoantibodies against type I IFNs in patients with life-threatening COVID-19. Science *370*, eabd4585. https://doi.org/10.1126/science.abd4585.
13. Habibi, M.S., Thwaites, R.S., Chang, M., Jozwik, A., Paras, A., Kirsebom, F., Varese, A., Owen, A., Cuthbertson, L., James, P., et al. (2020). Neutrophilic inflammation in the respiratory mucosa predisposes to RSV infection. Science *370*, eaba9301. https://doi.org/10.1126/science.aba9301.
14. Ordovas-Montanes, J., Beyaz, S., Rakoff-Nahoum, S., and Shalek, A.K. (2020). Distribution and storage of inflammatory memory in barrier tissues. Nat. Rev. Immunol. *20*, 308–320. https://doi.org/10.1038/s41577-019-0263-z.
15. Weisberg, S.P., Ural, B.B., and Farber, D.L. (2021). Tissue-specific immunity for a changing world. Cell *184*, 1517–1529. https://doi.org/10.1016/j.cell.2021.01.042.
16. Zhang, Q., Bastard, P., Liu, Z., Le Pen, J.L., Moncada-Velez, M., Chen, J., Ogishi, M., Sabli, I.K.D., Hodeib, S., Korol, C., et al. (2020). Inborn errors of type I IFN immunity in patients with life-threatening COVID-19. Science *370*, eabd4570. https://doi.org/10.1126/science.abd4570.
17. Wickenhagen, A., Sugrue, E., Lytras, S., Kuchi, S., Noerenberg, M., Turnbull, M.L., Loney, C., Herder, V., Allan, J., Jarmson, I., et al. (2021). A prenylated dsRNA sensor protects against severe COVID-19. Science *374*, eabj3624. https://doi.org/10.1126/science.abj3624.
18. Johnson, P.R., Jr., Feldman, S., Thompson, J.M., Mahoney, J.D., and Wright, P.F. (1985). Comparison of long-term systemic and secretory antibody responses in children given live, attenuated, or inactivated influenza A vaccine. J. Med. Virol. *17*, 325–335. https://doi.org/10.1002/jmv.1890170405.
19. Johnson, P.R., Feldman, S., Thompson, J.M., Mahoney, J.D., and Wright, P.F. (1986). Immunity to Influenza A Virus Infection in Young Children: A Comparison of Natural Infection, Live Cold-Adapted Vaccine, and Inactivated Vaccine. J. Infect. Dis. *154*, 121–127. https://doi.org/10.1093/infdis/154.1.121.
20. Rutigliano, J.A., Morris, M.Y., Yue, W., Keating, R., Webby, R.J., Thomas, P.G., and Doherty, P.C. (2010). Protective Memory Responses Are Modulated by Priming Events prior to Challenge. J. Virol. *84*, 1047–1056. https://doi.org/10.1128/JVI.01535-09.
21. Pizzolla, A., Nguyen, T.H.O., Smith, J.M., Brooks, A.G., Kedzieska, K., Heath, W.R., Reading, P.C., and Wakim, L.M. (2017). Resident memory CD8+ T cells in the upper respiratory tract prevent pulmonary influenza virus infection. Sci. Immunol. *2*, eaam6970. https://doi.org/10.1126/sciimmunol.aam6970.
22. Liew, F., Talwar, S., Cross, A., Willett, B.J., Scott, S., Logan, N., Siggins, M.K., Swieboda, D., Sidhu, J.K., Efstathiou, C., et al. (2023). SARS-CoV-2-specific nasal IgA wanes 9 months after hospitalisation with COVID-19

and is not induced by subsequent vaccination. EBiomedicine *87*, 104402. https://doi.org/10.1016/j.ebiom.2022.104402.

23. Sterlin, D., Mathian, A., Miyara, M., Mohr, A., Anna, F., Claër, L., Quentric, P., Fadlallah, J., Devilliers, H., Ghillani, P., et al. (2021). IgA dominates the early neutralizing antibody response to SARS-CoV-2. Sci. Transl. Med. *13*, eabd2223. https://doi.org/10.1126/scitranslmed.abd2223.
24. Wellford, S.A., Moseman, A.P., Dao, K., Wright, K.E., Chen, A., Plevin, J.E., Liao, T.-C., Mehta, N., and Moseman, E.A. (2022). Mucosal plasma cells are required to protect the upper airway and brain from infection. Immunity *55*, 2118–2134.e6. https://doi.org/10.1016/j.immuni.2022.08.017.
25. Weltzin, R., Traina-Dorge, V., Soike, K., Zhang, J.Y., Mack, P., Soman, G., Drabik, G., and Monath, T.P. (1996). Intranasal Monoclonal IgA Antibody to Respiratory Syncytial Virus Protects Rhesus Monkeys against Upper and Lower Respiratory Tract Infection. J. Infect. Dis. *174*, 256–261. https://doi.org/10.1093/infdis/174.2.256.
26. Morens, D.M., Taubenberger, J.K., and Fauci, A.S. (2023). Rethinking next-generation vaccines for coronaviruses, influenzaviruses, and other respiratory viruses. Cell Host Microbe *31*, 146–157. https://doi.org/10.1016/j.chom.2022.11.016.
27. Russell, M.W., Moldoveanu, Z., Ogra, P.L., and Mestecky, J. (2020). Mucosal Immunity in COVID-19: A Neglected but Critical Aspect of SARS-CoV-2 Infection. Front. Immunol. *11*, 611337. https://doi.org/10.3389/fimmu.2020.611337.
28. Lavelle, E.C., and Ward, R.W. (2022). Mucosal vaccines — fortifying the frontiers. Nat. Rev. Immunol. *22*, 236–250. https://doi.org/10.1038/s41577-021-00583-2.
29. Iwasaki, A., and Medzhitov, R. (2015). Control of adaptive immunity by the innate immune system. Nat. Immunol. *16*, 343–353. https://doi.org/10.1038/ni.3123.
30. Kadoki, M., Patil, A., Thaiss, C.C., Brooks, D.J., Pandey, S., Deep, D., Alvarez, D., von Andrian, U.H., Wagers, A.J., Nakai, K., et al. (2017). Organism-Level Analysis of Vaccination Reveals Networks of Protection across Tissues. Cell *171*, 398–413.e21. https://doi.org/10.1016/j.cell.2017.08.024.
31. Kaufmann, E., Sanz, J., Dunn, J.L., Khan, N., Mendonça, L.E., Pacis, A., Tzelepis, F., Pernet, E., Dumaine, A., Grenier, J.-C., et al. (2018). BCG Educates Hematopoietic Stem Cells to Generate Protective Innate Immunity against Tuberculosis. Cell *172*, 176–190.e19. https://doi.org/10.1016/j.cell.2017.12.031.
32. Ols, S., Yang, L., Thompson, E.A., Pushparaj, P., Tran, K., Liang, F., Lin, A., Eriksson, B., Karlsson Hedestam, G.B., Wyatt, R.T., and Loré, K. (2020). Route of Vaccine Administration Alters Antigen Trafficking but Not Innate or Adaptive Immunity. Cell Rep. *30*, 3964–3971.e7. https://doi.org/10.1016/j.celrep.2020.02.111.
33. Schenkel, J.M., Fraser, K.A., Beura, L.K., Pauken, K.E., Vezys, V., and Masopust, D. (2014). T cell memory. Resident memory CD8 T cells trigger protective innate and adaptive immune responses. Science *346*, 98–101. https://doi.org/10.1126/science.1254536.
34. Ariotti, S., Hogenbirk, M.A., Dijkgraaf, F.E., Visser, L.L., Hoekstra, M.E., Song, J.-Y., Jacobs, H., Haanen, J.B., and Schumacher, T.N. (2014). Skin-resident memory CD8+ T cells trigger a state of tissue-wide pathogen alert. Science *346*, 101–105. https://doi.org/10.1126/science.1254803.
35. McMaster, S.R., Wilson, J.J., Wang, H., and Kohlmeier, J.E. (2015). Airway-Resident Memory CD8 T Cells Provide Antigen-Specific Protection against Respiratory Virus Challenge through Rapid IFN-γ Production. J. Immunol. *195*, 203–209. https://doi.org/10.4049/jimmunol.1402975.
36. Steinbach, K., Vincenti, I., Kreutzfeldt, M., Page, N., Muschaweckh, A., Wagner, I., Drexler, I., Pinschewer, D., Korn, T., and Merkler, D. (2016). Brain-resident memory T cells represent an autonomous cytotoxic barrier to viral infection. J. Exp. Med. *213*, 1571–1587. https://doi.org/10.1084/jem.20151916.
37. Bosch-Camós, L., Alonso, U., Esteve-Codina, A., Chang, C.-Y., Martín-Mur, B., Accensi, F., Muñoz, M., Navas, M.J., Dabad, M., Vidal, E., et al. (2022). Cross-protection against African swine fever virus upon intranasal vaccination is associated with an adaptive-innate immune crosstalk. PLoS Pathog. *18*, e1010931. https://doi.org/10.1371/journal.ppat.1010931.
38. Stary, G., Olive, A., Radovic-Moreno, A.F., Gondek, D., Alvarez, D., Basto, P.A., Perro, M., Vrbanac, V.D., Tager, A.M., Shi, J., et al. (2015). VACCINES. A mucosal vaccine against Chlamydia trachomatis generates two waves of protective memory T cells. Science *348*, aaa8205. https://doi.org/10.1126/science.aaa8205.
39. Yao, Y., Jeyanathan, M., Haddadi, S., Barra, N.G., Vaseghi-Shanjani, M., Damjanovic, D., Lai, R., Afkhami, S., Chen, Y., Dvorkin-Gheva, A., et al. (2018). Induction of Autonomous Memory Alveolar Macrophages Requires T Cell Help and Is Critical to Trained Immunity. Cell *175*, 1634–1650.e17. https://doi.org/10.1016/j.cell.2018.09.042.
40. Boudreau, C.M., and Alter, G. (2019). Extra-Neutralizing FcR-Mediated Antibody Functions for a Universal Influenza Vaccine. Front. Immunol. *10*, 440. https://doi.org/10.3389/fimmu.2019.00440.
41. Klinkhammer, J., Schnepf, D., Ye, L., Schwaderlapp, M., Gad, H.H., Hartmann, R., Garcin, D., Mahlakõiv, T., and Staeheli, P. (2018). IFN-λ prevents influenza virus spread from the upper airways to the lungs and limits virus transmission. eLife *7*, e33354. https://doi.org/10.7554/eLife.33354.
42. Gonzalez, R.J., Hanč, P., Alvarez, D., Kazer, S.W., Messou, M.-A., Mazo, I.B., Match, C.M., Garg, R., Helble, J.D., Pallis, P., et al. (2024). Constitutive immune surveillance of nasal mucosa by three neutrophil subsets with distinct origin, phenotype, and function. Preprint at bioRxiv. https://doi.org/10.1101/2024.03.06.583781.
43. Boyd, D.F., Allen, E.K., Randolph, A.G., Guo, X.J., Weng, Y., Sanders, C.J., Bajracharya, R., Lee, N.K., Guy, C.S., Vogel, P., et al. (2020). Exuberant fibroblast activity compromises lung function via ADAMTS4. Nature *587*, 466–471. https://doi.org/10.1038/s41586-020-2877-5.
44. Bouvier, N.M., and Lowen, A.C. (2010). Animal Models for Influenza Virus Pathogenesis and Transmission. Viruses *2*, 1530–1563. https://doi.org/10.3390/v20801530.
45. Manicassamy, B., Manicassamy, S., Belicha-Villanueva, A., Pisanelli, G., Pulendran, B., and García-Sastre, A. (2010). Analysis of in vivo dynamics of influenza virus infection in mice using a GFP reporter virus. Proc. Natl. Acad. Sci. USA *107*, 11531–11536. https://doi.org/10.1073/pnas.0914994107.
46. Steuerman, Y., Cohen, M., Peshes-Yaloz, N., Valadarsky, L., Cohn, O., David, E., Frishberg, A., Mayo, L., Bacharach, E., Amit, I., and Gat-Viks, I. (2018). Dissection of Influenza Infection In Vivo by Single-Cell RNA Sequencing. Cell Syst. *6*, 679–691.e4. https://doi.org/10.1016/j.cels.2018.05.008.
47. Matsuoka, Y., Lamirande, E.W., and Subbarao, K. (2009). The mouse model for influenza. Curr Protoc Microbiol. Curr. Protoc. Microbiol. *Chapter 15*, Unit.15G.3. https://doi.org/10.1002/9780471729259.mc15g03s13.
48. Ibricevic, A., Pekosz, A., Walter, M.J., Newby, C., Battaile, J.T., Brown, E.G., Holtzman, M.J., and Brody, S.L. (2006). Influenza Virus Receptor Specificity and Cell Tropism in Mouse and Human Airway Epithelial Cells. J. Virol. *80*, 7469–7480. https://doi.org/10.1128/JVI.02677-05.
49. Deprez, M., Zaragosi, L.-E., Truchi, M., Becavin, C., Ruiz García, S., Arguel, M.-J., Plaisant, M., Magnone, V., Lebrigand, K., Abelanet, S., et al. (2020). A Single-Cell Atlas of the Human Healthy Airways. Am. J. Respir. Crit. Care Med. *202*, 1636–1645. https://doi.org/10.1164/rccm.201911-2199OC.
50. Ualiyeva, S., Lemire, E., Wong, C., Perniss, A., Boyd, A.A., Avilés, E.C., Minichetti, D.G., Maxfield, A., Roditi, R., Matsumoto, I., et al. (2024). A nasal cell atlas reveals heterogeneity of tuft cells and their role in directing olfactory stem cell proliferation. Sci. Immunol. *9*, eabq4341. https://doi.org/10.1126/sciimmunol.abq4341.

51. Brann, D.H., Tsukahara, T., Weinreb, C., Lipovsek, M., Van den Berge, K., Gong, B., Chance, R., Macaulay, I.C., Chou, H.-J., Fletcher, R.B., et al. (2020). Non-neuronal expression of SARS-CoV-2 entry genes in the olfactory system suggests mechanisms underlying COVID-19-associated anosmia. Sci. Adv. *6*, eabc5801. https://doi.org/10.1126/sciadv.abc5801.

52. Ziegler, C.G.K., Allon, S.J., Nyquist, S.K., Mbano, I.M., Miao, V.N., Tzouanas, C.N., Cao, Y., Yousif, A.S., Bals, J., Hauser, B.M., et al. (2020). SARS-CoV-2 Receptor ACE2 Is an Interferon-Stimulated Gene in Human Airway Epithelial Cells and Is Detected in Specific Cell Subsets across Tissues. Cell *181*, 1016–1035.e19. https://doi.org/10.1016/j.cell.2020.04.035.

53. Kochs, G., García-Sastre, A., and Martínez-Sobrido, L. (2007). Multiple Anti-Interferon Actions of the Influenza A Virus NS1 Protein. J. Virol. *81*, 7011–7021. https://doi.org/10.1128/JVI.02581-06.

54. Major, J., Crotta, S., Llorian, M., McCabe, T.M., Gad, H.H., Priestnall, S.L., Hartmann, R., and Wack, A. (2020). Type I and III interferons disrupt lung epithelial repair during recovery from viral infection. Science *369*, 712–717. https://doi.org/10.1126/science.abc2061.

55. Broggi, A., Ghosh, S., Sposito, B., Spreafico, R., Balzarini, F., Lo Cascio, A., Clementi, N., De Santis, M., Mancini, N., Granucci, F., et al. (2020). Type III interferons disrupt the lung epithelial barrier upon viral recognition. Science *369*, 706–712. https://doi.org/10.1126/science.abc3545.

56. Takaba, H., Morishita, Y., Tomofuji, Y., Danks, L., Nitta, T., Komatsu, N., Kodama, T., and Takayanagi, H. (2015). Fezf2 Orchestrates a Thymic Program of Self-Antigen Expression for Immune Tolerance. Cell *163*, 975–987. https://doi.org/10.1016/j.cell.2015.10.013.

57. Montoro, D.T., Haber, A.L., Biton, M., Vinarsky, V., Lin, B., Birket, S.E., Yuan, F., Chen, S., Leung, H.M., Villoria, J., et al. (2018). A revised airway epithelial hierarchy includes CFTR-expressing ionocytes. Nature *560*, 319–324. https://doi.org/10.1038/s41586-018-0393-7.

58. Lin, B., Shah, V.S., Chernoff, C., Sun, J., Shipkovenska, G.G., Vinarsky, V., Waghray, A., Xu, J., Leduc, A.D., Hintschich, C.A., et al. (2024). Airway hillocks are injury-resistant reservoirs of unique plastic stem cells. Nature *629*, 869–877. https://doi.org/10.1038/s41586-024-07377-1.

59. Grieshaber-Bouyer, R., Radtke, F.A., Cunin, P., Stifano, G., Levescot, A., Vijaykumar, B., Nelson-Maney, N., Blaustein, R.B., Monach, P.A., and Nigrovic, P.A.; ImmGen Consortium (2021). The neutrotime transcriptional signature defines a single continuum of neutrophils across biological compartments. Nat. Commun. *12*, 2856. https://doi.org/10.1038/s41467-021-22973-9.

60. Xie, X., Shi, Q., Wu, P., Zhang, X., Kambara, H., Su, J., Yu, H., Park, S.-Y., Guo, R., Ren, Q., et al. (2020). Single-cell transcriptome profiling reveals neutrophil heterogeneity in homeostasis and infection. Nat. Immunol. *21*, 1119–1133. https://doi.org/10.1038/s41590-020-0736-z.

61. Slütter, B., Pewe, L.L., Kaech, S.M., and Harty, J.T. (2013). Lung Airway-Surveilling CXCR3hi Memory CD8+ T Cells Are Critical for Protection against Influenza A Virus. Immunity *39*, 939–948. https://doi.org/10.1016/j.immuni.2013.09.013.

62. Wein, A.N., McMaster, S.R., Takamura, S., Dunbar, P.R., Cartwright, E.K., Hayward, S.L., McManus, D.T., Shimaoka, T., Ueha, S., Tsukui, T., et al. (2019). CXCR6 regulates localization of tissue-resident memory CD8 T cells to the airways. J. Exp. Med. *216*, 2748–2762. https://doi.org/10.1084/jem.20181308.

63. Liu, S.-Y., Sanchez, D.J., Aliyari, R., Lu, S., and Cheng, G. (2012). Systematic identification of type I and type II interferon-induced antiviral factors. Proc. Natl. Acad. Sci. USA *109*, 4239–4244. https://doi.org/10.1073/pnas.1114981109.

64. Moriyama, M., Chen, I.-Y., Kawaguchi, A., Koshiba, T., Nagata, K., Takeyama, H., Hasegawa, H., and Ichinohe, T. (2016). The RNA- and TRIM25-Binding Domains of Influenza Virus NS1 Protein Are Essential for Suppression of NLRP3 Inflammasome-Mediated Interleukin-1β Secretion. J. Virol. *90*, 4105–4114. https://doi.org/10.1128/JVI.00120-16.

65. Zhang, H., Alford, T., Liu, S., Zhou, D., and Wang, J. (2022). Influenza virus causes lung immunopathology through down-regulating PPARγ activity in macrophages. Front. Immunol. *13*, 958801. https://doi.org/10.3389/fimmu.2022.958801.

66. Mack, M., Cihak, J., Simonis, C., Luckow, B., Proudfoot, A.E.I., Plachý, J., Brühl, H., Frink, M., Anders, H.J., Vielhauer, V., et al. (2001). Expression and Characterization of the Chemokine Receptors CCR2 and CCR5 in Mice1. J. Immunol. *166*, 4697–4704. https://doi.org/10.4049/jimmunol.166.7.4697.

67. Schneider, M.A., Brühl, H., Wechselberger, A., Cihak, J., Stangassinger, M., Schlöndorff, D., and Mack, M. (2005). In vitro and in vivo properties of a dimeric bispecific single-chain antibody IgG-fusion protein for depletion of CCR2+ target cells in mice. Eur. J. Immunol. *35*, 987–995. https://doi.org/10.1002/eji.200425512.

68. Hufford, M.M., Kim, T.S., Sun, J., and Braciale, T.J. (2015). The Effector T Cell Response to Influenza Infection. In Influenza Pathogenesis and Control. Curr. Top. Microbiol. Immunol., *II*, M.B.A. Oldstone and R.W. Compans, eds. (Springer International Publishing), pp. 423–455. https://doi.org/10.1007/82_2014_397.

69. Jiang, X., Clark, R.A., Liu, L., Wagers, A.J., Fuhlbrigge, R.C., and Kupper, T.S. (2012). Skin infection generates non-migratory memory CD8+ TRM cells providing global skin immunity. Nature *483*, 227–231. https://doi.org/10.1038/nature10851.

70. Milner, J.J., Toma, C., Yu, B., Zhang, K., Omilusik, K., Phan, A.T., Wang, D., Getzler, A.J., Nguyen, T., Crotty, S., et al. (2017). Runx3 programs CD8+ T cell residency in non-lymphoid tissues and tumours. Nature *552*, 253–257. https://doi.org/10.1038/nature24993.

71. Crowl, J.T., Heeg, M., Ferry, A., Milner, J.J., Omilusik, K.D., Toma, C., He, Z., Chang, J.T., and Goldrath, A.W. (2022). Tissue-resident memory CD8+ T cells possess unique transcriptional, epigenetic and functional adaptations to different tissue environments. Nat. Immunol. *23*, 1121–1131. https://doi.org/10.1038/s41590-022-01229-8.

72. Rossen, R.D., Butler, W.T., Waldman, R.H., Alford, R.H., Hornick, R.B., Togo, Y., and Kasel, J.A. (1970). The Proteins in Nasal Secretion: II. A Longitudinal Study of IgA and Neutralizing Antibody Levels in Nasal Washings From Men Infected With Influenza Virus. JAMA *211*, 1157–1161. https://doi.org/10.1001/jama.211.7.1157.

73. Woof, J.M., and Mestecky, J. (2005). Mucosal immunoglobulins. Immunol. Rev. *206*, 64–82. https://doi.org/10.1111/j.0105-2896.2005.00290.x.

74. MacLean, A.J., Richmond, N., Koneva, L., Attar, M., Medina, C.A.P., Thornton, E.E., Gomes, A.C., El-Turabi, A., Bachmann, M.F., Rijal, P., et al. (2022). Secondary influenza challenge triggers resident memory B cell migration and rapid relocation to boost antibody secretion at infected sites. Immunity *55*, 718–733.e8. https://doi.org/10.1016/j.immuni.2022.03.003.

75. Lovell, D., Pawlowsky-Glahn, V., Egozcue, J.J., Marguerat, S., and Bähler, J. (2015). Proportionality: A Valid Alternative to Correlation for Relative Data. PLoS Comput. Biol. *11*, e1004075. https://doi.org/10.1371/journal.pcbi.1004075.

76. Quinn, T.P., Erb, I., Richardson, M.F., and Crowley, T.M. (2018). Understanding sequencing data as compositions: an outlook and review. Bioinformatics *34*, 2870–2878. https://doi.org/10.1093/bioinformatics/bty175.

77. Raredon, M.S.B., Yang, J., Kothapalli, N., Lewis, W., Kaminski, N., Niklason, L.E., and Kluger, Y. (2023). Comprehensive visualization of cell–cell interactions in single-cell and spatial transcriptomics with NICHES. Bioinformatics *39*, btac775. https://doi.org/10.1093/bioinformatics/btac775.

78. Gardai, S.J., Xiao, Y.-Q., Dickinson, M., Nick, J.A., Voelker, D.R., Greene, K.E., and Henson, P.M. (2003). By Binding SIRPα or Calreticulin/CD91, Lung Collectins Act as Dual Function Surveillance Molecules to Suppress or Enhance Inflammation. Cell *115*, 13–23. https://doi.org/10.1016/S0092-8674(03)00758-X.

79. Denning, N.-L., Aziz, M., Murao, A., Gurien, S.D., Ochani, M., Prince, J.M., and Wang, P. (2020). Extracellular CIRP as an endogenous TREM-1 ligand to fuel inflammation in sepsis. JCI Insight *5*, e134172. https://doi.org/10.1172/jci.insight.134172.

80. Morgan, A.J., Guillen, C., Symon, F.A., Birring, S.S., Campbell, J.J., and Wardlaw, A.J. (2008). CXCR6 identifies a putative population of retained human lung T cells characterised by co-expression of activation markers. Immunobiology *213*, 599–608. https://doi.org/10.1016/j.imbio.2008.01.005.

81. Dumm, R.E., Wellford, S.A., Moseman, E.A., and Heaton, N.S. (2020). Heterogeneity of Antiviral Responses in the Upper Respiratory Tract Mediates Differential Non-lytic Clearance of Influenza Viruses. Cell Rep. *32*, 108103. https://doi.org/10.1016/j.celrep.2020.108103.

82. Adamson, M.S., Nesic, S., Buness, A., Bayrak, K., Schmitz, S., Soler, S., Zillinger, T., Marx, S., Lambing, S., Andryka-Cegielski, K., et al. (2022). RIG-I activation primes and trains innate antiviral immune memory. Preprint at bioRxiv. https://doi.org/10.1101/2022.10.27.514004.

83. Ordovas-Montanes, J., Dwyer, D.F., Nyquist, S.K., Buchheit, K.M., Vukovic, M., Deb, C., Wadsworth, M.H., Hughes, T.K., Kazer, S.W., Yoshimoto, E., et al. (2018). Allergic inflammatory memory in human respiratory epithelial progenitor cells. Nature *560*, 649–654. https://doi.org/10.1038/s41586-018-0449-8.

84. Lercher, A., Cheong, J.-G., Jiang, C., Hoffmann, H.-H., Ashbrook, A.W., Yin, Y.S., Quirk, C., DeGrace, E.J., Chiriboga, L., Rosenberg, B.R., et al. (2023). Antiviral innate immune memory in alveolar macrophages following SARS-CoV-2 infection. Preprint at bioRxiv. https://doi.org/10.1101/2023.11.24.568354.

85. Cheong, J.-G., Ravishankar, A., Sharma, S., Parkhurst, C.N., Grassmann, S.A., Wingert, C.K., Laurent, P., Ma, S., Paddock, L., Miranda, I.C., et al. (2023). Epigenetic memory of coronavirus infection in innate immune cells and their progenitors. Cell *186*, 3882–3902.e24. https://doi.org/10.1016/j.cell.2023.07.019.

86. Aegerter, H., Kulikauskaite, J., Crotta, S., Patel, H., Kelly, G., Hessel, E.M., Mack, M., Beinke, S., and Wack, A. (2020). Influenza-induced monocyte-derived alveolar macrophages confer prolonged antibacterial protection. Nat. Immunol. *21*, 145–157. https://doi.org/10.1038/s41590-019-0568-x.

87. Iijima, N., and Iwasaki, A. (2014). T cell memory. A local macrophage chemokine network sustains protective tissue-resident memory CD4 T cells. Science *346*, 93–98. https://doi.org/10.1126/science.1257530.

88. Clark, R.A., Chong, B., Mirchandani, N., Brinster, N.K., Yamanaka, K.I., Dowgiert, R.K., and Kupper, T.S. (2006). The Vast Majority of CLA+ T Cells Are Resident in Normal Skin1. J. Immunol. *176*, 4431–4439. https://doi.org/10.4049/jimmunol.176.7.4431.

89. Tse, S.-W., Radtke, A.J., Espinosa, D.A., Cockburn, I.A., and Zavala, F. (2014). The Chemokine Receptor CXCR6 Is Required for the Maintenance of Liver Memory CD8+ T Cells Specific for Infectious Pathogens. J. Infect. Dis. *210*, 1508–1516. https://doi.org/10.1093/infdis/jiu281.

90. Heim, T.A., Lin, Z., Steele, M.M., Mudianto, T., and Lund, A.W. (2023). CXCR6 promotes dermal CD8+ T cell survival and transition to long-term tissue residence. Preprint at bioRxiv. https://doi.org/10.1101/2023.02.14.528487.

91. Smillie, C.S., Biton, M., Ordovas-Montanes, J., Sullivan, K.M., Burgin, G., Graham, D.B., Herbst, R.H., Rogel, N., Slyper, M., Waldman, J., et al. (2019). Intra- and Inter-cellular Rewiring of the Human Colon during Ulcerative Colitis. Cell *178*, 714–730.e22. https://doi.org/10.1016/j.cell.2019.06.029.

92. Zheng, H.B., Doran, B.A., Kimler, K., Yu, A., Tkachev, V., Niederlova, V., Cribbin, K., Fleming, R., Bratrude, B., Betz, K., et al. (2021). A Treatment-Naïve Cellular Atlas of Pediatric Crohn's Disease Predicts Disease Severity and Therapeutic Response. Preprint at medRxiv. https://doi.org/10.1101/2021.09.17.21263540.

93. Darrah, P.A., Zeppa, J.J., Maiello, P., Hackney, J.A., Wadsworth, M.H., Hughes, T.K., Pokkali, S., Swanson, P.A., Grant, N.L., Rodgers, M.A., et al. (2020). Prevention of tuberculosis in macaques after intravenous BCG immunization. Nature *577*, 95–102. https://doi.org/10.1038/s41586-019-1817-8.

94. Zhang, K., Erkan, E.P., Jamalzadeh, S., Dai, J., Andersson, N., Kaipio, K., Lamminen, T., Mansuri, N., Huhtinen, K., Carpén, O., et al. (2022). Longitudinal single-cell RNA-seq analysis reveals stress-promoted chemoresistance in metastatic ovarian cancer. Sci. Adv. *8*, eabm1831. https://doi.org/10.1126/sciadv.abm1831.

95. Chen, K., Zhang, J., Huang, Y., Tian, X., Yang, Y., and Dong, A. (2022). Single-cell RNA-seq transcriptomic landscape of human and mouse islets and pathological alterations of diabetes. iScience *25*, 105366. https://doi.org/10.1016/j.isci.2022.105366.

96. Li, H., Wang, X., Wang, Y., Zhang, M., Hong, F., Wang, H., Cui, A., Zhao, J., Ji, W., and Chen, Y.-G. (2022). Cross-species single-cell transcriptomic analysis reveals divergence of cell composition and functions in mammalian ileum epithelium. Cell Regen. *11*, 19. https://doi.org/10.1186/s13619-022-00118-7.

97. Cao, Y., Lin, Y., Ormerod, J.T., Yang, P., Yang, J.Y.H., and Lo, K.K. (2019). scDC: single cell differential composition analysis. BMC Bioinformatics *20*, 721. https://doi.org/10.1186/s12859-019-3211-9.

98. Büttner, M., Ostner, J., Müller, C.L., Theis, F.J., and Schubert, B. (2021). scCODA is a Bayesian model for compositional single-cell data analysis. Nat. Commun. *12*, 6876. https://doi.org/10.1038/s41467-021-27150-6.

99. Dann, E., Henderson, N.C., Teichmann, S.A., Morgan, M.D., and Marioni, J.C. (2022). Differential abundance testing on single-cell data using k-nearest neighbor graphs. Nat. Biotechnol. *40*, 245–253. https://doi.org/10.1038/s41587-021-01033-z.

100. Gloor, G.B., Macklaim, J.M., Pawlowsky-Glahn, V., and Egozcue, J.J. (2017). Microbiome Datasets Are Compositional: And This Is Not Optional. Front. Microbiol. *8*, 2224. https://doi.org/10.3389/fmicb.2017.02224.

101. Lin, H., and Peddada, S.D. (2020). Analysis of microbial compositions: a review of normalization and differential abundance analysis. npj Biofilms Microbiomes *6*, 60. https://doi.org/10.1038/s41522-020-00160-w.

102. Aitchison, J., Barceló-Vidal, C., Martín-Fernández, J.A., and Pawlowsky-Glahn, V. (2000). Logratio Analysis and Compositional Distance. Math. Geol. *32*, 271–275. https://doi.org/10.1023/A:1007529726302.

103. Hu, M.-W., Kim, D.W., Liu, S., Zack, D.J., Blackshaw, S., and Qian, J. (2019). PanoView: an iterative clustering method for single-cell RNA sequencing data. PLoS Comput. Biol. *15*, e1007040. https://doi.org/10.1371/journal.pcbi.1007040.

104. Patterson-Cross, R.B., Levine, A.J., and Menon, V. (2021). Selecting single cell clustering parameter values using subsampling-based robustness metrics. BMC Bioinformatics *22*, 39. https://doi.org/10.1186/s12859-021-03957-4.

105. Zheng, H.B., Doran, B.A., Kimler, K., Yu, A., Tkachev, V., Niederlova, V., Cribbin, K., Fleming, R., Bratrude, B., Betz, K., et al. (2023). Concerted changes in the pediatric single-cell intestinal ecosystem before and after anti-TNF blockade. eLife *12*, RP91792. https://doi.org/10.7554/eLife.91792.1.

106. Rutigliano, J.A., Sharma, S., Morris, M.Y., Oguin, T.H., McClaren, J.L., Doherty, P.C., and Thomas, P.G. (2014). Highly Pathological Influenza A Virus Infection Is Associated with Augmented Expression of PD-1 by Functionally Compromised Virus-Specific CD8+ T Cells. J. Virol. *88*, 1636–1651. https://doi.org/10.1128/JVI.02851-13.

107. Hao, Y., Hao, S., Andersen-Nissen, E., Mauck, W.M., Zheng, S., Butler, A., Lee, M.J., Wilk, A.J., Darby, C., Zager, M., et al. (2021). Integrated analysis of multimodal single-cell data. Cell *184*, 3573–3587.e29. https://doi.org/10.1016/j.cell.2021.04.048.

108. Quinn, T.P., Richardson, M.F., Lovell, D., and Crowley, T.M. (2017). propr: An R-package for Identifying Proportionally Abundant Features Using Compositional Data Analysis. Sci. Rep. *7*, 16252. https://doi.org/10.1038/s41598-017-16520-0.

109. Trombetta, J.J., Gennert, D., Lu, D., Satija, R., Shalek, A.K., and Regev, A. (2014). Preparation of Single-Cell RNA-Seq Libraries for Next Generation Sequencing. Curr. Protoc. Mol. Biol. *107*, 4.22.1–4.22.17. https://doi.org/10.1002/0471142727.mb0422s107.

110. Li, B., Gould, J., Yang, Y., Sarkizova, S., Tabaka, M., Ashenberg, O., Rosen, Y., Slyper, M., Kowalczyk, M.S., Villani, A.-C., et al. (2020). Cumulus provides cloud-based data analysis for large-scale single-cell and single-nucleus RNA-seq. Nat. Methods *17*, 793–798. https://doi.org/10.1038/s41592-020-0905-x.

111. Fleming, S.J., Chaffin, M.D., Arduini, A., Akkad, A.-D., Banks, E., Marioni, J.C., Philippakis, A.A., Ellinor, P.T., and Babadi, M. (2022). Unsupervised removal of systematic background noise from droplet-based single-cell experiments using CellBender. Preprint at bioRxiv. https://doi.org/10.1101/791699.

112. Jung, S.-H., Hwang, B.-H., Shin, S., Park, E.-H., Park, S.-H., Kim, C.W., Kim, E., Choo, E., Choi, I.J., Swirski, F.K., et al. (2022). Spatiotemporal dynamics of macrophage heterogeneity and a potential function of Trem2hi macrophages in infarcted hearts. Nat. Commun. *13*, 4580. https://doi.org/10.1038/s41467-022-32284-2.

113. Ratnasiri, K., Wilk, A.J., Lee, M.J., Khatri, P., and Blish, C.A. (2023). Single-cell RNA-seq methods to interrogate virus-host interactions. Semin. Immunopathol. *45*, 71–89. https://doi.org/10.1007/s00281-022-00972-2.

114. Angerer, P., Haghverdi, L., Büttner, M., Theis, F.J., Marr, C., and Buettner, F. (2016). destiny: diffusion maps for large-scale single-cell data in R. Bioinformatics *32*, 1241–1243. https://doi.org/10.1093/bioinformatics/btv715.

115. Linderman, G.C., Zhao, J., Roulis, M., Bielecki, P., Flavell, R.A., Nadler, B., and Kluger, Y. (2022). Zero-preserving imputation of single-cell RNA-seq data. Nat. Commun. *13*, 192. https://doi.org/10.1038/s41467-021-27729-z.

116. Türei, D., Korcsmáros, T., and Saez-Rodriguez, J. (2016). OmniPath: guidelines and gateway for literature-curated signaling pathway resources. Nat. Methods *13*, 966–967. https://doi.org/10.1038/nmeth.4077.

117. Xu, C., Lopez, R., Mehlman, E., Regier, J., Jordan, M.I., and Yosef, N. (2021). Probabilistic harmonization and annotation of single-cell transcriptomics data with deep generative models. Mol. Syst. Biol. *17*, e9620. https://doi.org/10.15252/msb.20209620.

Please cite this article in press as: Kazer et al., Primary nasal influenza infection rewires tissue-scale memory response dynamics, Immunity (2024), https://doi.org/10.1016/j.immuni.2024.06.005

STAR★METHODS

KEY RESOURCES TABLE

REAGENT or RESOURCE	SOURCE	IDENTIFIER
Antibodies		
TotalSeq™-B0301 anti-mouse Hashtag 1 Antibody	Biolegend	Cat#155831; Clones M1/42, 30-F11; RRID: AB_2814067
TotalSeq™-B0302 anti-mouse Hashtag 2 Antibody	Biolegend	Cat#155833; Clones M1/42, 30-F11; RRID: AB_2814068
TotalSeq™-B0303 anti-mouse Hashtag 3 Antibody	Biolegend	Cat#155835; Clones M1/42, 30-F11; RRID: AB_2814069
CCR2, APC	R&D Systems	Cat#FAB5538A-100; Clone 475301
CD3ε, Alexa Fluor® 488	Biolegend	Cat#100321; Clone 145-2C11; RRID: AB_389300
CD11b, Alexa Fluor® 594	Biolegend	Cat#101254; Clone M1/70; RRID: AB_2563231
CD19, Alexa Fluor® 488	Biolegend	Cat#115521; Clone 6D5; RRID: AB_389307
CD19, Brilliant Violet 421™	Biolegend	Cat#115538; Clone 6D5; RRID: AB_11203527
CD19, Brilliant Violet 650™	Biolegend	Cat#115541; Clone 6D5; RRID: AB_11204087
CD3ε, Alexa Fluor® 700	Biolegend	Cat#152316; Clone 500A2; RRID: AB_2632713
CD4, Brilliant Violet 421™	Biolegend	Cat#100438; Clone GK1.5; RRID: AB_11203718
CD8b, PerCP/Cyanine5.5	Biolegend	Cat#126610; Clone YTS156.7.7; RRID: AB_2260149
CD45, APC/Cyanine7	Biolegend	Cat#103116; Clone 30-F11; RRID: AB_312981
CD45, Alexa Fluor® 488	Biolegend	Cat#103122; Clone 30-F11; RRID: AB_493531
CD45, Brilliant Violet 605™	Biolegend	Cat#103139; Clone 30-F11; RRID: AB_2562341
CD45, Brilliant Violet 650™	Biolegend	Cat#103151; Clone 30-F11; RRID: AB_2565884
CD45, PE	Biolegend	Cat#103106; Clone 30-F11; RRID: AB_312971
CD64 (FcγRI), APC	Biolegend	Cat#139306; Clone X54-5/7.1; RRID: AB_11219391
CD69, APC	Biolegend	Cat#104514; Clone H1.2F3; RRID: AB_492843
CD103, PE	Biolegend	Cat#121406; Clone 2E7; RRID: AB_1133989
CD274 (PD-L1), PE	Biolegend	Cat#124308; Clone 10F.9G2; RRID: AB_2073556
CD326 (Ep-CAM), Alexa Fluor® 488	Biolegend	Cat#118210; Clone G8.8; RRID: AB_1134099
CD326 (Ep-CAM), Alexa Fluor® 594	Biolegend	Cat#118222; Clone G8.8; RRID: AB_2563322
CD326 (Ep-CAM), Alexa Fluor® 647	Biolegend	Cat#118212; Clone G8.8; RRID: AB_1134101
CD326 (Ep-CAM), Biotin	Biolegend	Cat#118204; Clone G8.8; RRID: AB_1134178
F4/80, Brilliant Violet 421™	Biolegend	Cat#123137; Clone BM8; RRID: AB_2563102
Cytokeratin 13 (KRT13), Alexa Fluor® 488	Abcam	Cat#ab198584; Clone EPR3671
Cytokeratin 13 (KRT13), Alexa Fluor® 647	Abcam	Cat#ab198585; Clone EPR3671
IgA, PE, eBioscience™	Invitrogen	Cat#12-4204-82; Clone mA-6E1; RRID: AB_465917
Ig, κ Light Chain, BV421	BD Biosciences	Cat#562888; Clone 187.1; RRID: AB_2737867
Ig, λ1, λ2 & λ3 Light Chain, BV421	BD Biosciences	Cat#744523; Clone R26-46; RRID: AB_2742297
Ly-6C, PerCP/Cyanine5.5	Biolegend	Cat#128012; Clone HK1.4; RRID: AB_1659241
Ly-6G, APC/Cyanine7	Biolegend	Cat#127624; Clone 1A8; RRID: AB_10640819
MHC-II (I-A/I-E), Alexa Fluor® 700	Biolegend	Cat#107621; Clone M5/114.15.2; RRID: AB_493726
MHC-II (I-A/I-E), Brilliant Violet 421™	Biolegend	Cat#107632; Clone M5/114.15.2; RRID: AB_2650896
NK-1.1, Alexa Fluor® 488	Biolegend	Cat#108718; Clone PK136; RRID: AB_493183
NK-1.1, PE/Cyanine7	Biolegend	Cat#108714; Clone PK136; RRID: AB_389364
Influenza A virus NS1, non-conjugated (rabbit)	ThermoFisher	Cat#PA5-32243; RRID: AB_2549716
Anti-Rabbit Goat IgG (H+L), Alexa Fluor® 488	Invitrogen	Cat#A-11034; RRID: AB_2576217
Acetyl-α-Tubulin (Lys40), unconjugated (rabbit)	Cell Signaling Technology	Cat# 5335S; Clone D20G3
Anti-Rabbit F(ab')2-Donkey IgG (H+L), PE	Invitrogen	Cat# 12-4739-81; RRID: AB_1210761

(*Continued on next page*)

Please cite this article in press as: Kazer et al., Primary nasal influenza infection rewires tissue-scale memory response dynamics, Immunity (2024), https://doi.org/10.1016/j.immuni.2024.06.005

Continued

REAGENT or RESOURCE	SOURCE	IDENTIFIER
CCR2 (MC-21), depleting antibody	Provided by Matthias Mack (Univeristät Regensburg)	N/A
Ultra-LEAF™ Purified Rat IgG2b, κ Isotype Ctrl	Biolegend	Cat#400644; RTK4530; RRID: AB_11149687
Bacterial and virus strains		
A/Puerto Rico/8/1934 (PR8), influenza A virus	Provided by Daniel Lingwood (Ragon Institute of Mass General, MIT, and Harvard)	N/A
A/HKx31 (X31), influenza A virus	Provided by Daniel Lingwood (Ragon Institute of Mass General, MIT, and Harvard)	N/A
Chemicals, peptides, and recombinant proteins		
Liberase™ TL	Millipore Sigma	Cat#5401020001
DNase I	Roche	Cat#11284932001
Dynabeads™ Biotin Binder	Invitrogen	Cat#11047
Buffer RLT	Qiagen	Cat#79216
Dulbecco's modified eagle's medium	Corning	Cat#10-017-CV
Fetal bovine serum	Gemini	Cat#100-106
Penicillin:Streptomycin (100x)	Gemini	Cat#400109
Iscove's DMEM	Corning	Cat#10-016-CV
Bovine serum albumin	EMD Millipore	Cat#EM-2960
TPCK treated Trypsin	Millipore Sigma	Cat#T1426
Zirconia/Silica beads, 2.3mm	Biospec Products	Cat#11079125z
HEPES, 1M	Corning	Cat#25-060-CI
Hank's Balanced Salt Solution (HBSS)	Corning	Cat#21-021-CV
2-Mercaptoethanol	Millipore Sigma	Cat#M6250
Critical commercial assays		
RNeasy Mini Kit	Qiagen	Cat#74104
TaqMan™ Fast Advanced Master Mix for qPCR	ThermoFisher Scientific	Cat#4444556
Ifnb1 qpcr probe	ThermoFisher Scientific	Cat#Mm00439552_s1
Ifng qpcr probe	ThermoFisher Scientific	Cat#Mm01168134_m1
Ifnl3 qpcr probe	ThermoFisher Scientific	Cat#Mm00663660_g1
gentleMACS™ M Tube	Miltenyi Biotec	Cat#130-093-236
AccuCheck Counting Beads	Invitrogen	Cat#PCB100
Chromium Next GEM Single Cell 3' Kit v3.1, 16 rxns	10x Genomics	Cat#1000268
Chromium Next GEM Chip G Single Cell Kit, 48 rxns	10x Genomics	Cat#1000120
3' Feature Barcode Kit, 16 rxns	10x Genomics	Cat#1000261
Dual Index Kit NT Set A, 96 rxn	10x Genomics	Cat#1000242
Dual Index Kit TT Set A 96 rxns	10x Genomics	Cat#1000215
RNAscope® Multiplex Fluorescent Reagent Kit v2	ACD	Cat#323270
RNAscope® 4-Plex Ancillary kit	ACD	Cat#323120
RNAscope® Probe - Mm-Krt13	ACD	Cat#575341
RNAscope® Probe - Mm-Cxcr6-C2	ACD	Cat#871991-C2
RNAscope® Probe - Mm-Cxcl16-C3	ACD	Cat#466681-C3
RNAscope® Probe - Mm-Cd274-C3	ACD	Cat#420501-C3
Opal 520	Akoya Biosciences	Cat#FP1487001KT
Opal 570	Akoya Biosciences	Cat#FP1488001KT
Opal 690	Akoya Biosciences	Cat#FP1497001KT

(*Continued on next page*)

Please cite this article in press as: Kazer et al., Primary nasal influenza infection rewires tissue-scale memory response dynamics, Immunity (2024), https://doi.org/10.1016/j.immuni.2024.06.005

Continued

REAGENT or RESOURCE	SOURCE	IDENTIFIER
VECTASHIELD PLUS	Vector Laboratories	Cat#H-1900
eBioscience™ Foxp3 / Transcription Factor Staining Buffer Set	Invitrogen	Cat#00-5523-00
LIVE/DEAD Fixable Aqua Dead Cell Stain	Invitrogen	Cat#L34957
Deposited data		
FASTQ, raw h5, and hashtag count csv files	This paper	GEO: GSE266469
Processed count matrices	This paper	Single Cell Portal: SCP2216, SCP2221
Experimental models: Cell lines		
Madin-Darby canine kidney (MDCK) cells	Provided by Daniel Lingwood	N/A
Experimental models: Organisms/strains		
C57BL/6J	The Jackson Laboratory	Cat#000664; RRID: IMSR_JAX:000664
Software and algorithms		
Original code	This paper	https://doi.org/10.5281/zenodo.11104940
Seurat v4.2.1	Hao et al.[107]	https://satijalab.org/seurat/
propr v4.2.6	Quinn et al.[108]	https://github.com/tpq/propr
Cytoscape v3.9.1	Cytoscape Consortium	https://cytoscape.org/
NICHES v1.0.0	Raredon et al.[77]	https://github.com/msraredon/NICHES

RESOURCE AVAILABILITY

Lead contact

Further information and requests for resources should be directed to and will be fulfilled by the lead contact, Jose Ordovas-Montanes (jose.ordovas-montanes@childrens.harvard.edu).

Materials availability

The mouse line used in this study is available from Jackson Laboratories. The anti-CCR2 antibody MC-21 was provided as a gift by Prof. Matthias Mack. This study did not generate new unique reagents.

Data and code availability

All raw sequencing data and aligned single-cell RNA-seq files are publicly available at GEO and the annotated and processed data are publicly available at Broad Institute Single Cell Portal (https://singlecell.broadinstitute.org) as of the date of publication. Accession numbers are listed in the key resources table. All original code is available as of the date of publication. The DOI is listed in the key resources table. Any additional information required to reanalyze the data reported in this paper is available from the lead contact upon request.

EXPERIMENTAL MODEL AND STUDY PARTICIPANT DETAILS

Mice

All experiments were approved by the Harvard University Institutional Animal Care and Use Committee and run following NIH guidelines. Female C57BL/6J (B6) mice 6 to 8 weeks old were purchased from The Jackson Laboratory and experiments commenced 1 to 3 weeks following their arrival. Three (3) mice per timepoint were infected with 10^4 pfu IAV PR8 in a 10μL volume that was administered by pipette dropwise to the nares to allow each drop to be inhaled (5μl/nostril). Mice were restrained during this administration but not anesthetized, to maintain the virus in the upper respiratory tract. For rechallenge experiments, mice previously inoculated with 10^4 pfu PR8 were administered with either 10^4 pfu PR8 or 10^5 pfu X31 60 days after the initial PR8 infection. A higher dose of X31 was used in rechallenge given its reduced pathology.[106] All mice were housed in a BSL-2+ facility with specific pathogen free conditions.

METHOD DETAILS

Virus growth, quantification, and infections

IAV strain A/Puerto Rico/8/1934 (PR8) and Madin-Darby canine kidney (MDCK) cells were generously provided by Dr. Daniel Lingwood and Dr. Maya Sangesland of the Ragon Institute of Mass General, MIT, and Harvard. Virus was propagated and quantified in MDCK cells. MDCK cells were grown at 37°C with 5% CO_2 in cell growth media: Dulbecco's modified eagle's medium (DMEM), 10% fetal bovine serum (FBS), 1X Penicillin:Streptomycin. PR8 was grown in MDCK cells in influenza growth media: Iscove's DMEM, 0.2%

Please cite this article in press as: Kazer et al., Primary nasal influenza infection rewires tissue-scale memory response dynamics, Immunity (2024), https://doi.org/10.1016/j.immuni.2024.06.005

bovine serum albumin (BSA; EMD Millipore, EM-2960), 1X Penicillin:Streptomycin, and 2μg/mL TPCK treated Trypsin (Sigma, T1426).

For viral load quantification experiments, mice were sacrificed in CO_2 and lungs and heads were separated. For the nasal cavity, fur and skin were removed and the lower jaws cut off. The entire nasal cavity or lungs were collected into 1mL PBS with 2.3mm Zirconia/Silica beads and stored on ice. The tissue was homogenized in an OMNI Bead Ruptor Elite at 3m/s for 30 seconds twice, centrifuged 500g for 5 minutes, and supernatant was collected and stored at -80°C until thawed for plaque assays. Virus titers were measured by plaque assays in confluent MDCK cells in 6-well plates. MDCK cells were grown in cell growth media, washed with sterile phosphate-buffered saline (PBS), then washed with influenza growth media. Media was removed and serial dilutions of viral supernatant in influenza growth media were added to each well in a 400μL volume, incubated for 1 hour at 37°C, then overlayed with 0.3% agarose in influenza growth media. Infected cells were incubated for three days at 37°C, fixed with 4% paraformaldehyde, stained with crystal violet, washed, and plaques were counted.

Sample processing for single-cell RNA-seq

Three separate regions of the nasal tissue were harvested independently: (1) the respiratory mucosa (RM), (2) the olfactory mucosa (OM), and (3) the lateral nasal gland (LNG). The nasal tissue was collected by removing the skin and connective tissue from around the head, cutting off the lower jaw, and opening the nasal cavity by peeling away the nasal bone from the rest of the skull. Tissue separation and collection was performed using a dissection scope with a 4x objective. All nasal tissue surrounding the nasoturbinates, maxillary turbinates, and septum, including the mucosa that runs along the nasal lateral walls between the nasoturbinates and maxillary turbinate, and the mucosal tissue under the nasal bone that connects the nasoturbinates and septum, were collected together and constitute the RM. After removal of the RM the ethmoid turbinates were collected including both the mucosal tissue and the bone and cartilage of the turbinates, but not the surrounding skull, constituting the OM. After removal of the OM, the LNG was exposed and could be collected without any bone or cartilage. The nasal-associated lymphoid tissue (NALT) was not collected in any of the three regions. Matched RM, OM, and LNG regions were collected simultaneously from the three mice per timepoint, and each timepoint was processed on a different day.

Each nasal tissue region was collected into 750μL Wash Media (RPMI 1640, 2% FBS, 10 mM HEPES, and 1X Penicillin:Streptomycin) and stored on ice. Tissues were chopped with scissors then 750μL Digestion Media (Wash Media with 100μg/mL Liberase and 100μg/mL of DNAse I) was added. Tissues were incubated at 37°C with end-over-end rotation, 30 minutes for RM and OM, 20 minutes for LNG. 13.3μL EDTA (0.5M) was added to each sample and then cells were washed with HBSS Media (HBSS (Ca, Mg Free), 10mM EDTA, 10mM HEPES, 2% FBS) and filtered through a 70μm nylon cell strainer. Cells were pelleted by centrifugation 500g for 10 minutes, resuspended with ACK (Ammonium-Chloride-Potassium) lysis buffer for 1 minute on ice, and then diluted with 9mL HBSS Media and centrifuged 500g for 5 minutes twice. Cells were then resuspended in 1mL Isolation Buffer (PBS, 0.1% BSA, 2mM EDTA) pre-mixed with 25μL anti-EpCAM-biotin-Dynabeads (anti-EpCAM-biotin antibody bound to Dynabeads Biotin Binder) for a light epithelial cell depletion, incubated for 15 minutes on ice, washed with Isolation Buffer and placed on a Dynamag for 2 minutes. Supernatants were collected, centrifuged 500g for 5 minutes, resuspended in 100μL Staining Buffer (PBS, 1% BSA, 0.01% Tween) and 10μL Fc block, and incubated on ice for 10 minutes. Next, 0.5μg Biolegend TotalSeq Hashing antibodies B0301, B0302, or B0303 were added so that each mouse had all three nasal regions (RM, OM, and LNG) stained with one of the three antibodies, and incubated on ice for 20 minutes. Cells were then washed extensively to remove excess antibody with 10mL Staining Buffer and centrifugation at 500g for 5 minutes twice. Cells were resuspended in Loading Buffer (PBS and 0.04% BSA), counted, and pooled equally (13,500 cells/sample) between three mice for each region. Finally, each set of pooled cells were centrifuged 500g for 5 minutes and resuspended in 42μl Loading Buffer for downstream scRNA-seq processing.

As stated above, we chose to increase the relative proportion of non-epithelial cells in our scRNA-seq dataset, by performing a partial EpCAM depletion using magnetic beads. This decision was made following experiments comparing this approach to undepleted RM tissue in naïve mice; we found that while depletion reduced the relative abundance of some epithelial cell clusters, it did not result in the complete loss of any cluster. Thus, the cellular compositions throughout the study represent the nasal mucosa tissue after both dissociation and epithelial cell depletion and, therefore, do not reflect the true frequencies of cell types within intact nasal mucosa. Nevertheless, our atlas can still be used to assign cell cluster labels to new datasets where epithelial cells have not been depleted and will inform spatial transcriptomics approaches to derive more accurate cell abundances in vivo.

Single-cell RNA-seq

Pooled samples from each nasal region (RM, OM, and LNG) were processed using the 10x Genomics Chromium Next GEM Single Cell 3' Kit v3.1 and Feature Barcoding Kit with dual indices per the manufacturer's instructions. Approximately 40,000 cells per pooled reaction were loaded on the 10x Genomics Chromium Controller. Library quality was evaluated using the Agilent TapeStation 4200 (Agilent). Prior to sequencing, the gene expression and hashtag libraries were pooled 20:1. Sequencing was performed on either the NovaSeq 6000 or NextSeq 2000 (Illumina) with an average RNA read depth of 16,000 reads/cell and hashtag read depth of 500 reads/cell.

Immunofluorescence Microscopy

Mice were euthanized in CO_2 and their heads following skin, fur, and lower jaw removal were placed in 4% paraformaldehyde for 1-4 hours on ice for fixation. Heads were transferred to 0.5M EDTA for 2-3 days at 4°C for bone decalcification. Heads were transferred to

Please cite this article in press as: Kazer et al., Primary nasal influenza infection rewires tissue-scale memory response dynamics, Immunity (2024), https://doi.org/10.1016/j.immuni.2024.06.005

30% sucrose in PBS for cryoprotection for 2 days at 4°C then rapidly frozen in NEG-50 using dry ice. Frozen heads were stored at -20°C until cryostat sectioning. Mouse nasal tissues were cut into 50-100μm sections, permeabilized with 0.3% Tween in PBS (PBST) for 1 hour, then incubated overnight at 4°C with antibodies, DAPI, and Fc block at a 1:200 dilution in PBST. Antibodies used: anti-Influenza A virus NS1 (PA5-32243, ThermoFisher), anti-acetyl-α-tubulin (Ly640, D20G3, Cell Signaling Technology), anti-CD45 (30-F11, Biolegend), anti-EpCAM (G8.8, Biolegend), anti-Krt13 (EPR3671, Abcam), anti-PD-L1 (10F.9G2, Biolegend), and anti-IgA (mA-6E1, ThermoFisher). Samples were then washed 3 times with PBST in 15-minute intervals at room temperature, mounted on glass slides with Prolong Gold, and visualized with an Olympus FLUOVIEW FV3000 confocal laser scanning microscope.

qPCR

RM tissue was collected as described above from mice and lysed in Buffer RLT + 1% beta-mercaptoethanol via gentleMACS Octo Dissociator in M-Tubes (Miltenyi Biotec). RNA was extracted from tissue lysate by RNAEasy Mini column purification following the manufacturer's instructions. cDNA was then generated following the SmartSeq II protocol as previously described.[109] qPCR was performed using TaqMan reagents and probes on a CFX384 Real-Time PCR System.

Antibody-based depletion

Naïve or PR8 infected B6 mice were administered daily 20μg anti-CCR2 depleting antibodies (MC-21 generously provided by Prof. Matthias Mack, Universität Regensburg) or rat IgG2b,κ isotype control intraperitoneally (i.p.) as advised by its provider. 24h following one administration, blood was collected from naïve mice by tail vein bleed into FACS buffer (PBS, 0.5% BSA, 2mM EDTA) and stored on ice before processing for flow cytometry.

PR8 infected mice were administered antibodies 3, 4, and 5 dpi in 24h intervals. For this experiment, mice were euthanized at 8 dpi.

Flow cytometry

Blood was processed for flow cytometry by pelleting cells by centrifugation and resuspending with ACK lysis buffer to remove RBCs. Cells were then washed with FACS buffer and stained in 50 μL for flow cytometry using the following antibodies: anti-CCR2 (APC), anti-CD11b (AF594), anti-CD19 (BV421), anti-CD3e (AF488), anti-CD45 (BV605), anti-Ly6C (PerCP-Cy5.5), anti-Ly6G (APC-Cy7), and anti-NK1.1 (PE-Cy7). Cells were analyzed using the Beckman Coulter CytoFLEX.

For RM tissue, mice were anesthetized i.p. with ketamine (100 mg/kg body weight) and xylazine (10 mg/kg body weight) prior to euthanasia and administered 1μg anti-CD45 antibody (PE, APC/Cy7) by retroorbital intravascular injection to label CD45+ cells in circulation. Mice were then euthanized 3 minutes later in CO_2. RM tissue was processed as described above for tissue harvesting and single-cell suspension preparation through ACK lysis and dilution. Cells were then centrifuged and resuspended in 100 μL FACS buffer LIVE/DEAD Fixable Aqua Dead Cell Stain per manufacturer's instructions. Cells were then washed and stained for 30min at 4°C in the dark with Fc block diluted 1:200 and subsets of the following antibodies: anti-CD103 (PE), anti-CD11b (AF594), anti-CD11c (PE/Cy7), anti-CD19 (AF488, BV650), anti-CD3e (AF488, AF700), anti-CD4 (BV421), anti-CD45 (BV605), anti-CD64 (APC), anti-CD69 (APC), anti-CD8b (PerCP/Cy5.5), anti-CD326 (AF488, AF594), anti-Ly6C (PerCP/Cy5.5), anti-Ly6G (APC/Cy7), anti-F4/80 (BV421), anti-MHC-II (AF700, BV421), and anti-NK1.1 (AF488). To stain for Krt13, IgA, and IgK/L intracellularly, cells were fixed and permeabilized using the eBioscience Transcription Factor Staining Buffer Set according to the manufacturer's instructions. Cells were stained with anti-Krt13 (AF647) at 1:250, or anti-IgA (PE), anti-IgK (BV421), and anti-IgL (BV421) at 1:100. Following staining, cells were washed in FACS buffer, and analyzed. To determine cell counts, AccuCheck Counting Beads were added to every sample.

RNAscope Microscopy

RNA *in situ* hybridization was performed according to manufacturer's instructions for the RNAscope Multiplex Fluorescent Reagent Kit v2 (Advanced Cell Diagnostics ACD, 323270) on 20 μm thin sections of fixed-frozen murine nasal mucosa tissue collected 14 dpi. We implemented the following modifications to preserve tissue integrity: 1) 5 min PBS wash preceding initial baking of slides was removed; 2) slides were baked for 30 min at 60°C following EtOH dehydration; 3) target retrieval time was reduced to 5 min; 4) slides were baked for 60 min at 60°C following target retrieval; and 5) tissue sections were incubated in Protease Plus instead of Protease III for milder protease digestion. Probes used included Mm-Krt13, Mm-Cxcr6-C2, Mm-Cxcl16-C3, and Mm-Cd274-C3. Following signal amplification, Opal 520, Opal 570, and Opal 690 dyes were used, diluted 1:1000 in TSA buffer. Nuclei were stained with DAPI and slides were mounted with VECTASHIELD PLUS. Confocal images were collected using an Olympus FLUOVIEW FV3000 confocal laser scanning microscope.

QUANTIFICATION AND STATISTICAL ANALYSIS

Single-cell RNA-seq pre-processing

To detect reads originating from IAV, we built a combined genome of mm10 (GRCm39) and the sequences for PR8 (NCBI Taxonomy ID #211044). The eight PR8 genomic viral segment sequences (NC_002023.1, NC_002022.1, NC_002021.1, NC_002020.1, NC_00219.1, NC_2018.1, NC_002017.1, and NC_002016.1) and associated IAV gene annotations were added to the GRCm39 FASTA and GTF files and processed using the CellRanger's built in "mkref" function. Sequences were then aligned and quantified using this combined genome with the CellRanger toolkit (v6.0.1) via Cumulus tools[110] (https://cumulus.readthedocs.io/en/stable/).

Please cite this article in press as: Kazer et al., Primary nasal influenza infection rewires tissue-scale memory response dynamics, Immunity (2024), https://doi.org/10.1016/j.immuni.2024.06.005

Cell sample identity was assigned from the measurement of TotalSeqB aligned counts using the cumulus demultiplexing tool for feature barcoding, calling identity for any cell with at least 100 barcodes. To correct for transcript spill-over, cellbender[111] was applied to the raw output UMI matrices from CellRanger with the following parameters: *expected_cells=30000*, *fpr=0.01, total_droplets_included=50000*. Cellbender corrected cells were then filtered based on Unique Molecular Identifiers (UMI) count (>750 & <10000), number of detected genes (>500), and percentage of mitochondrial genes (<15%). Finally, cells labeled as doublets by demultiplexing were removed.

Clustering, annotation, and IAV+ cell calling

Downstream analysis was performed using Seurat (v.4.2.1).[107] Briefly, the entire primary infection dataset underwent normalization using the *scTransform* function followed by principal component analysis (PCA), shared nearest neighbors (SNN) graph generation, Louvain clustering, and UMAP embedding. Clustering was performed at multiple resolutions to help annotate similar and dissimilar clusters. Using clustering *resolution = 0.6*, cluster specific/enriched markers were calculated. Each cluster was labeled by major cell type based on the expression of known lineage markers (e.g., *Omp*, *Epcam*, *Ptprc, Flt1*, etc.). Doublet clusters were also annotated based on the lack of unique markers and/or the presence of multiple mutually exclusive lineage markers (e.g., *Omp+Ptprc+* cells). Following annotation, doublet clusters were removed, and the normalization/clustering/doublet removal process was repeated twice more (total of three times) until no doublet clusters were discernable.

The dataset was then divided into separate objects by cell type label for further subclustering. Following the same routine applied to the full dataset, clusters for each cell type were annotated with subset/state labels based on prior knowledge and previously published scRNAseq datasets of the nasal mucosa.[10,50,51] After the first set of annotations in every cell type object, it was apparent that there were still intra-sample doublets present: mostly contaminating cell types, but also within cell type doublets (e.g., ionocyte/sustentacular doublets). These clusters were iteratively removed like in the analysis of the full dataset, for a total of three rounds in each cell type, yielding a total of 127 clusters across the whole dataset. To visualize these clusters' relationships and distribution across nasal regions, we built a cell cluster "phylogenetic tree" using ARBOL,[92] where the first tier encodes major cell type, the second tier encodes defined subtypes, and the third tier encodes cluster identity (Figure S1F). We note that succinctly depicting relative proportions of the data across multiple replicates is complex; stacked bar charts like Figure 1D show relative proportions within a cell type grouping, but do not reflect proportions within the cells captured at each timepoint/region.

For epithelial cells, we categorized clusters into broader subsets including basal (*Krt5, Krt14*), ciliated (*Foxj1, Dnah5*), serous (*Ltf*, *Ccl9*), glandular (*Bpifb9b, Odam*), goblet/secretory (*Reg3g, Selenom, Scgb1c1*, and mucin-encoding genes), ionocyte (*Cftr, Coch*), tuft (*Trpm5, Il25*), and sustentacular cells (*Sec14l3, Cyp2g1*) in addition to the rarer clusters without clear lineages. For neutrophils, we annotated a differentiation trajectory starting with granulocyte-myeloid precursor like cells (*Elane, Mpo*), differentiating through immature states (*Camp, Mmp8, Retnlg*), and ending with several clusters of mature neutrophils (*Il1b, H2-D1, Siglecf*). Additionally, mast cells expressing *Il6*, *Gata2*, and *Il4* were found in small numbers. For myeloid cells we characterized several macrophage (*Cd74, C1qb, Ccl4*) clusters including a *Trem2+* subset expressing *Fcrls, Il1a*, and *Pf4* (CXCL4), an innate immune recruiting subset expressing *Ccl7, Ccl8*, and *Pf4* (CXCL4), and a small cluster of osteoclasts (*Ctsk, Mmp9*). Monocytes clustered into classical (*Ly6c2, Ccr2, Chil3*) and non-classical (*Ace*, *Ear2, Itgal*) subsets[112] alongside IFN-stimulated monocytes and monocyte-derived macrophages (MDMs). DCs separated into distinct clusters including Langerhans-like (*Epcam, Ccl17, Ccl22*), intraepithelial (*Cd103, Xcr1, Tlr3*), migratory (*Ccr7, Ccl22, Cd274*), and a subset uniquely expressing *Cd209a* (DC-SIGN), *Tnfsf9* (4-1BB), and *Klrd1*. We also captured plasmacytoid DCs (*Siglech, Irf8*; pDCs). Subclustering T and NK cells revealed NK cell subsets (*Klrb1c, Ncr1*), type 2 (*Areg, Il13*) and type 3 (*Il22, Rorc*) innate lymphoid cells (ILC), $\gamma\delta$T cells (*Trdc, Cd163l1, Cd3e*), and a spectrum of $\alpha\beta$T cell subsets and states including naïve/central memory CD8 (*Ccr7, Dapl1*), effector CD8 (*Gzmb, Gzmk*), T_{RM}-like CD8 cells (*Itgae* [CD103]), resting CD4 (*Cd4, Tnfrsf4* [OX40]), Th1 CD4 (*Ifng, Cd200*), Th17 (*Cd40lg, Il17a*), and a cluster of Helios (*Ikzf2*) expressing cells. B cell clustering revealed mature subsets (*Ighd, Cd74*), IgG+/IgA+ early plasmablast cells (*Aicda, Jchain, Igha*), lambda-chain-high expressing cells (*Iglc1, Iglc2*), nucleoside diphosphate kinase (NME) expressing cells (*Nme*1, *Nme2*) and, primarily in OM, developing subsets including pro-B (*Dntt, Vpreb1, Rag1*), pre-B (*Bub1b, Mki67, Sox4*), and immature B cells (*Ms4a1, Ifi30*).

We note that neurons, mostly olfactory sensory neurons, make up a large number of cells in our primary infection dataset (n > 50,000). Given their importance in mouse olfaction, and their broad distribution through the OE and OM (Figure 1B), we believe that their relative abundance in our scRNA-seq data is concordant with the anatomy and biology of the nasal mucosa.

IAV transcript capture was sparse in our dataset. Other studies have included spike-in primers to facilitate additional capture of viral nucleic acids[113]; it is possible that we were not sufficiently sensitive to IAV transcripts without these spike-in primers. Also, cells productively infected with virus may not be sufficiently viable through our tissue processing pipeline, as suggested by the viral reads detected by bulk RNA-seq from tissue lysate, leading to artificially low numbers of cells containing IAV reads. Thus, we classified IAV+ cells as any cell with 2 or more UMIs aligned to any IAV PR8 gene.

Compositional analyses

After removing multiplets, immune (>97.5%) and endothelial cells (89%) had nearly all cells assigned a sample replicate while neurons (30.7%), epithelial cells (65.9%), fibroblasts (52.4%), and other stromal cells (56.4%) had lower sample annotation rates (Figure S1E). We note that cells without a sample replicate assignment were excluded from all compositional analyses. Within cell type frequencies were calculated on a per replicate basis by counting the number of cells within each cluster label and dividing by the total number of cells for that cell type captured in that replicate. For tissue- and region-level compositional analyses, cell

Please cite this article in press as: Kazer et al., Primary nasal influenza infection rewires tissue-scale memory response dynamics, Immunity (2024), https://doi.org/10.1016/j.immuni.2024.06.005

cluster abundances were calculated by deriving cell cluster frequencies over all labeled cells in each sample replicate, scaling to 3,000 cells per replicate, and log transforming. Subsequent PCAs were calculated using the center-log ratio (clr) transformed data.

Proportionality analysis was performed using the propr package (v4.2.6).[108] We compared the proportionality statistic ρ, calculated from the clr transformed abundance data, to standard Pearson correlation across all pairwise comparisons and found ρ to be more stringent for significance cutoffs (FDR<0.05) generated by permutating testing (Figure S8A). We built a network using Cytoscape (v3.9.1) comprised of all significantly proportional cell cluster pairs to assess groups of cell clusters with similar cell abundance trajectories throughout the infection time course.

RM sample replicate distances were calculated using the Aitchison distance.[102] Euclidean distance on the clr transformed data then calculated between all pairs of RM sample replicates, yielding three distances within a timepoint and nine distances between two timepoints. Statistics on Aitchison distances were performed using a one-sided non-parametric Welch's ANOVA and Dunnett's T3 test for multiple comparisons in Prism.

Neutrophil pseudotime analysis

The neutrophil pseudotime analysis was performed using diffusion mapping as previously described.[59] A principal component analysis was run on all cells assigned to granulocyte clusters, excluding mast cells. The first 20 principal components were used to compute a cell-to-cell distance matrix using *1 – Pearson correlation coefficient* as the distance metric. Using the destiny package in R,[114] we computed a diffusion map with standard parameters with density normalization and rotate enabled. We manually selected "Progenitor" cells as the root of the trajectory and used the DPT function to calculate the pseudotime values, manually scaling the values from 0 to 1.

Cell-cell signaling analysis

Three cell networks (IFN-stimulated MDMs: *Gzmk*+ CD8 T cells: *Ifng*+*Cd200*+ CD4 T cells; Cd103+ DCs: *Dusp2*+*Icam1*+ mature neutrophils: *Gp2*+*Lyz2*+ goblet/secretory cells; *Krt13*+*Il1a*+ epithelial cells: *Cd103*+ CD8 T cells: CD4 T cells) were selected based on high proportionality throughout the primary infection time-course or specific biological interest to the authors. Data for the clusters of interest in each network were then subset to RM and timepoint of interest to best capture individual cells with sufficient spatial and temporal proximity to plausibly interact and re-normalized with Seurat's *NormalizeData* function. Since NICHES calculates the multiplicative expression of ligand-receptor pairs from a random sampling of cells from each cell type to predict cell-cell communication, Adaptively thresholded Low-Rank Approximation (ALRA) imputation was applied to each cell network to reduce the impact of technical zeros due to potential dropout events.[115] NICHES was then run on each cell network individually, drawing from the OmniPath database of ligand-receptor pairs[116] to generate a cell interaction object whereby rows are ligand-receptor pairs and columns are cell type pairs.[77] These objects were then scaled and passed through principal component analysis and UMAP dimensionality reduction to generate low-dimensional embeddings of cell interactions. Differentially expressed interactions were identified using the Seurat *FindAllMarkers* function, and highly differentially expressed interactions validated by literature review were selected for display as heatmaps.

RNAscope co-localization quantification

RNAscope quantification was carried out using ImageJ software on five fields of view (FOV) from both the naïve and 14 dpi timepoints (n = 5/timepoint). Ten slices were selected in the z-plane from each FOV to generate maximum intensity projections across 5 μm, and color channels were separated using the "Split Channels" function. For each image, a threshold was set for signal intensity in the *Krt13* channel, allowing generation of a mask of *Krt13* expression that was subsequently overlaid on both the DAPI and *Cxcl16* channels to generate regions of interest for further analysis. Within the region of interest in the DAPI channel, nuclei were manually counted with the aid of the ImageJ plugin "Cell Counter," with inclusion of most segmented nuclei. Within the region of interest in the *Cxcl16* channel, a threshold was set for *Cxcl16* expression with the aid of a signal intensity histogram and then punctuate dots were counted automatically with the "Analyze Particles" function. A measure of average *Cxcl16* puncta per DAPI-stained nuclei in the *Krt13*+ region was calculated for each FOV.

Label transfer validation and memory samples

To assign cluster labels to new scRNA-seq datasets generated from the nasal mucosa, we leveraged the structure of our data to test the label transfer methods provided in Seurat[107] and scANVI.[117] We separated the cells from one RM replicate from each timepoint as a query dataset, using the remaining cells as the reference. With Seurat, we implemented the FindTransferAnchors function on the scTransformed data, using the first 40 PCs from the PCA as the reference. Labels were then assigned with the TransferData function using either cell cluster or cell type identities. With scANVI, we first built a scVI model on the reference data, and then a scANVI model using either cell cluster or cell type identities as labels. The reference scANVI model was then used to train a model on the query data. We calculated the percentage of correctly called cell labels using each method for both sets of labels and found calling to be superior on the cell type level. Thus, we next repeated each procedure within each cell type to learn cell cluster labels and found Seurat to perform better across all cell types (89.11-95.19% correctly annotated using Seurat vs 69.33-92.31% using scANVI). Using Seurat, this approach was repeated with two other non-overlapping sets of sample replicates (one per timepoint) to assess reproducibility (Figures S7A and S7B). To further validate, we calculated cell cluster abundances using the predicted cell cluster labels for the query replicates and projected into the PCA calculated across the RM samples (Figure S7C).

Please cite this article in press as: Kazer et al., Primary nasal influenza infection rewires tissue-scale memory response dynamics, Immunity (2024), https://doi.org/10.1016/j.immuni.2024.06.005

We next applied the two-step label transfer approach using Seurat to new data generated from RM 60 dpi and 2 and 5 dprc. Before performing label transfer, we removed all hashtag annotated cell doublets from the new dataset and applied the same filtering criteria as above. We next performed *scTransform* and PCA on the new dataset. We then predicted cell type labels using all cells from RM samples in the primary infection dataset for reference. We next removed any cells from subsequent analysis that had a maximum prediction assignment score < 0.8 (i.e., 80% is the greatest confidence in label prediction), making up 5% of the total dataset. Given our loading strategy and number of intrasample doublets found in the primary infection dataset, we chose a more stringent cutoff following cell type label prediction. Separating into each cell type and using the processed data from the matching cell type in the primary infection dataset as reference, we performed the same procedure. Here, we were more liberal, keeping all cells with a maximum prediction assignment score ≥ 0.4 since very similar clusters within cell types could receive almost equal prediction probability (e.g., Resting Basal and Abi3bp Resting Basal). With cell cluster labels assigned, we then calculated cell cluster abundances as above and performed downstream differential expression analysis.

Since plasma cells were absent from our primary infection data and could not be identified by label transfer, we re-clustered all B cells across both datasets. We resolved a small cluster (n=75 cells) of plasma cells expressing *Slpi*, *Jchain*, *Igha*, and *Xbp1* present at low frequencies at 60 dpi and during rechallenge (Figures S7H and S7I).